






# Anisotropic structure of nanofiber hydrogel accelerates diabetic wound healing via triadic synergy of immune-angiogenic-neurogenic microenvironments

Kunkoo Kim<sup>a,1</sup>, Jia Yang<sup>a,1</sup>, Chengli Li<sup>b,1</sup>, Chun-Yi Yang<sup>a,c,\*\*</sup> , Peilun Hu<sup>b,d</sup>, Yaosai Liu<sup>b</sup>, Yin-yuan Huang<sup>a,e</sup> , Xiaohan Sun<sup>a</sup>, Ming Chi<sup>a</sup>, Chenyu Huang<sup>b</sup>, Xiaodan Sun<sup>a</sup>, Lingyun Zhao<sup>a</sup>, Xiumei Wang<sup>a,\*</sup> 

<sup>a</sup> State Key Laboratory of New Ceramics and Fine Processing, Key Laboratory of Advanced Materials, School of Materials Science and Engineering, Tsinghua University, 100084, Beijing, China

<sup>b</sup> Beijing Tsinghua Changgung Hospital, School of Clinical Medicine, Tsinghua University, 102218, Beijing, China

<sup>c</sup> Center for Biomaterials and Regenerative Medicine, Wuzhen Laboratory, 314500, Tongxiang, China

<sup>d</sup> Beijing Friendship Hospital, Capital Medical University, 102218, Beijing, China

<sup>e</sup> Department of Biomedical Engineering, Washington University in St. Louis, 63130, St. Louis, Missouri, United States

## ARTICLE INFO

### Keywords:

Anisotropic nanofiber hydrogel  
Self-assembling peptide  
Multicellular modulation  
Multidimensional microenvironment refinement  
Diabetic wound healing

## ABSTRACT

Wound healing in chronic diabetic patients remains challenging due to the multiple types of cellular dysfunction and the impairment of multidimensional microenvironments. The physical signals of structural anisotropy offer significant potential for orchestrating multicellular regulation through physical contact and cellular mechanosensing pathways, irrespective of cell type. In this study, we developed a highly oriented anisotropic nanofiber hydrogel designed to provide directional guidance for cellular extension and cytoskeletal organization, thereby achieving pronounced multicellular modulation, including shape-induced polarization of macrophages, morphogenetic maturation of Schwann cells, oriented extracellular matrix (ECM) deposition by fibroblasts, and enhanced vascularization by endothelial cells. Additionally, we incorporated a VEGF-mimicking peptide to further reinforce angiogenesis, a pivotal phase that interlocks with immune regulation, neurogenesis, and tissue regeneration, ultimately contributing to optimized inter-microenvironmental crosstalk. *In vivo* studies validated that the anisotropic bioactive nanofiber hydrogel effectively accelerated diabetic wound healing by harnessing the triadic synergy of the immune-angiogenic-neurogenic microenvironments. Our findings highlight the promising potential of combining physical and bioactive signals for the modulation of various cell types and the refinement of the multidimensional microenvironment, offering a novel strategy for diabetic wound healing.

## 1. Introduction

Diabetes is a chronic metabolic disorder affecting more than one in ten adults globally, leading to various complications and a diminished quality of life for patients [1]. Diabetic wounds are chronic and non-healing wounds characterized by a destructive microenvironment, often resulting in high medical costs and increased risks of amputation, thus posing a significant challenge for tissue repair [2]. Despite various

available therapies, including surgical debridement, wound offloading, negative pressure wound therapy, hyperbaric oxygen therapy, nerve decompression, and antibacterial-based therapy, clinical outcomes of diabetic wound healing remain unsatisfactory [3–5]. The wound healing process consists of complex and overlapping phases, including hemostasis, inflammation, proliferation, and remodeling [6], which are disrupted in diabetic wounds due to an imbalanced microenvironment, leading to prolonged healing [7]. The persistent hyperglycemic and

\* Corresponding author.

\*\* Corresponding author. State Key Laboratory of New Ceramics and Fine Processing, Key Laboratory of Advanced Materials, School of Materials Science and Engineering, Tsinghua University, 100084, Beijing, China.

E-mail addresses: [steve19940607@gmail.com](mailto:steve19940607@gmail.com) (C.-Y. Yang), [wxm@mail.tsinghua.edu.cn](mailto:wxm@mail.tsinghua.edu.cn) (X. Wang).

<sup>1</sup> These authors contributed equally to the work.

<https://doi.org/10.1016/j.bioactmat.2025.01.004>

Received 25 September 2024; Received in revised form 7 December 2024; Accepted 6 January 2025

2452-199X/© 2025 The Authors. Publishing services by Elsevier B.V. on behalf of KeAi Communications Co. Ltd. This is an open access article under the CC BY-NC-ND license (<http://creativecommons.org/licenses/by-nc-nd/4.0/>).

hypoxic microenvironment in diabetic wounds are primarily responsible for inducing severe oxidative stress, high infection risk, chronic inflammation, impaired vascularization, neuropathic complications, and various cellular dysfunctions, consequently constructing inhibitory microenvironments for delayed tissue regeneration. The complex pathological features of diabetic wounds limit the effectiveness of single-factor healing strategies due to the neglect of multiple cellular dysfunctions and the impairment of multidimensional microenvironments [8]. Therefore, therapeutic strategies that focus on modulating multiple cell types through bioactive materials are emerging as promising approaches for diabetic wound healing.

Biomaterials like hydrogels, can provide physical protection and support while delivering multi-modal signals, including physical, chemical, and bioactive cues, to guide cell behaviors [9–13]. Unlike those cell-specific biochemical signals, physical structure signals are capable of regulating the directly attached cells via physical contact and cellular mechano-sensing pathways, irrespective of cell type, manifesting the promising potential for diverse tissue regeneration [14–17]. Recently, fibrous scaffolds, such as nanofibril-sponge [18,19], nanofiber hydrogel film [20,21], and oriented fibrous hydrogel [22,23], have been extensively studied in wound healing due to their abilities to enhance moisture transport, improve cell adhesion, and provide diverse functionalization opportunities. Anisotropic structures, in particular, have been reported to significantly impact various cellular processes by providing aligned structural guidance for cytoskeletal extension and orientation, thereby demonstrating great potential for modulating multiple cell types [24,25]. Nonetheless, the use of biomaterials featuring anisotropic topography in skin tissue regeneration has not been extensively investigated. Given the inherently oriented assembly of cells and extracellular matrix in skin tissue, anisotropic signals may more effectively mimic natural tissue architecture, offering an optimal approach to promote wound healing through directional guidance and tension reduction [26]. Additionally, recent studies have demonstrated that anisotropic hydrogels can induce macrophage reprogramming, Schwann cell maturation, endothelial cell vascularization, and aligned collagen deposition, potentially addressing the critical cellular dysfunction features in diabetic wounds [27–30]. Nano-scaled topographical cues, when delivered at appropriate magnitudes, can maximize the cellular sensitivity towards structural signals, exhibiting remarkable effects on cell migration and organization, cellular function manipulation, and tissue microarchitecture guidance. In our previous studies, aligned fibrin nanofiber hydrogels (AFG) were fabricated via electrospinning and molecular self-assembly, presenting hierarchically oriented constructs with excellent biocompatibility, degradability, viscoelasticity, and cell-modulating capability [31]. We found that AFG could participate in the manipulation of mesenchymal stem cell (MSC) differentiation, rat dorsal root ganglion (DRG) neuron's axon guidance, Schwann cell maturation, microglia polarization, and neural stem cell (NSC) modulation, revealing the latent capacity for excellent cellular facilitation and tissue regeneration [32–36]. Such anisotropic nanofiber hydrogel can realize the multicellular modulation through prominent oriented structural signals, further regulating the specific microenvironment.

Beyond modulating individual microenvironment, the interaction between multidimensional microenvironments is essential for establishing a pro-regenerative environment. Angiogenesis, in particular, plays a pivotal role in mediating the crosstalk among the immune, neurogenic, and vascular microenvironments [8]. This process is intricately linked to the immune response, as angiogenesis facilitates immune cell recruitment and modulates inflammation, while the immune response, in turn, influences angiogenic progression [37]. Furthermore, endothelial and neural cells interact within the neurovascular niche, where angiogenesis and neurogenesis support each other through reciprocal signaling [38]. Hence, promoting angiogenesis emerges as a promising target to facilitate efficient crosstalk among these multidimensional microenvironments. Our previous work has demonstrated

that the VEGF-mimetic peptide KLTWQELYQLKYKGI (KLT), in combination with self-assembling motifs such as RADA16-I (RAD), effectively modulates angiogenesis [39]. Therefore, integrating KLT peptides into the aligned fibrin hydrogel as bioactive motifs, such functionalized anisotropic nanofiber hydrogel could modulate angiogenesis and further reinforced the crosstalk among multidimensional microenvironments, ultimately reconstructing a regenerative niche for diabetic wound healing.

In this study, we developed bioactive anisotropic fibrin hydrogels to deliver dual impacts of oriented structural and pro-angiogenic signals, accelerating diabetic wound healing via the triadic synergy of the immune-angiogenic-neurogenic microenvironment refinement (Fig. 1A). The anisotropic nanofiber hydrogel that was fabricated using electrospinning, exhibiting ideal fibrous alignment and pronounced multicellular modulating capability, induced endothelial cell vascularization, regulated macrophage phenotypic transition, promoted Schwann cell maturation, and enhanced fibroblast extracellular matrix (ECM) deposition. Further, the incorporation of KLT peptide reinforced the crosstalk among immune, vascular, and neural microenvironments, unveiling the potential for multidimensional microenvironment reconstruction *in vitro*. Subsequently, the regenerative efficiency of the bioactive aligned hydrogels was evaluated in a rat diabetic wound healing model. Histological results demonstrated significant optimization of the inflammatory, vascular, and neural microenvironments, reconstructing pro-regenerative niches for organized ECM remodeling, wound closure acceleration, and skin tissue regeneration. This study highlighted the application of anisotropic fibrous hydrogel in diabetic wound healing with multidimensional microenvironment optimization, providing new insights for advanced strategies in the clinical management of chronic wound healing.

## 2. Materials and methods

### 2.1. Fabrication of hydrogels

Aligned fibrin hydrogel (AFG) was fabricated by electrospinning as described previously. In brief, 4 % (w/v) fibrinogen (F8630, Sigma-Aldrich, USA) and 0.5 % (w/v) polyethylene oxide (PEO, 4000 kDa, Sigma-Aldrich, USA) were dissolved in distilled water respectively, and mixed in equal ratio for further fiber fabrication. The mixed solution was electrospun through a 21G needle under a voltage of 4 kV at a flow rate of 2.5 mL/h and harvested in a liquid bath of 50 mM CaCl<sub>2</sub> and 15 units/mL thrombin (T4648, Sigma-Aldrich, USA) on the rotating collector at a speed of 60 rpm. Subsequently, collected fibers were twinned on a circular Tetrafluoroethylene (PTFE) frame for further use. Remaining PEO was removed from fibers by washing with distilled water for 24 h. For sterilization, AFG hydrogels were exposed to ultraviolet light and immersed in 75 % ethanol for three days simultaneously. Random fibrin hydrogel (RFG) was prepared by adding 25 units/mL of thrombin in 50 mM CaCl<sub>2</sub> solution directly into 2 % (w/v) fibrinogen (F8630, Sigma-Aldrich, USA) to form a bulk hydrogel in a sterile environment.

The self-assembling VEGF-mimetic peptide KLT was synthesized as previously described by Scilight Biotechnology LLC (Ac-RADARADAR-ADARADA-GG-KLTWQELYQLKYKGI-NH<sub>2</sub>, purity >90 %, ChinaPeptides Co., Ltd., Shanghai, China). The peptide powders were dissolved in ultrapure water to form 1 % w/v concentration. Then, AFG and RFG were soaked in KLT solution (1 % w/v) for 20 min, and in the mixed solution of 0.4 mg/mL 1-ethyl-3-(dimethylaminopropyl) carbodiimide hydrochloride (EDC) (Sigma-Aldrich, USA) with 0.6 mg/mL N-hydroxysuccinimide (NHS) (Sigma-Aldrich, USA) for 30 min successively under sterile condition. Finally, hydrogels were rinsed with distilled water three times to generate KLT-functionalized AFG (AFG<sup>KLT</sup>) and RFG (RFG<sup>KLT</sup>). Hydrogels were equilibrated in phosphate buffered saline (PBS) before *in vitro* and *in vivo* application.

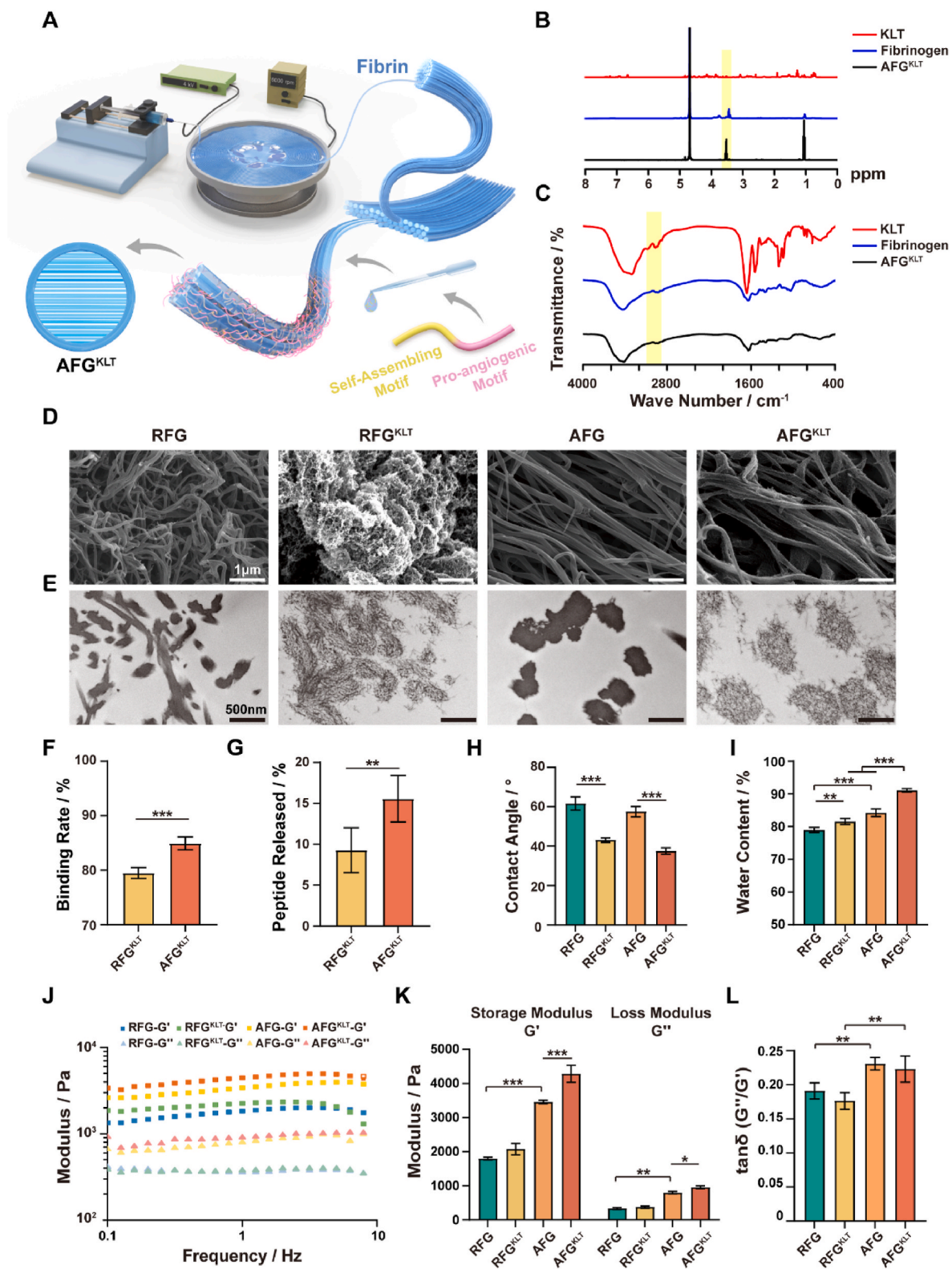


**Fig. 1.** Fabrication and characterization of AFG<sup>KLT</sup> hydrogel. A) Schematic illustration of electrospinning and self-assembling peptide conjugation for AFG<sup>KLT</sup> fabrication. B, C) <sup>1</sup>H NMR spectra (B) and FTIR spectra (C) of RAD/KLT peptide, fibrinogen, and AFG<sup>KLT</sup> hydrogel. D, E) Representative SEM (D) and TEM (E) images of RFG, RFG<sup>KLT</sup>, AFG, and AFG<sup>KLT</sup> hydrogels. F) The self-assembling binding rate of RAD/KLT peptides onto RFG and AFG hydrogels. G) The peptide-releasing profile of RFG<sup>KLT</sup> and AFG<sup>KLT</sup> hydrogels after 24 h cultivation in PBS at 37 °C. H) The contact angle of corresponding hydrogels. I) The water content of corresponding hydrogels. J) Rheological measurement of storage (G') and loss (G'') moduli of corresponding hydrogels in a frequency sweep (from 0.1 Hz to 10 Hz) at a constant strain of 1 %. K) The average storage and loss moduli of corresponding hydrogels at 1 Hz and 1 % strain. L) The average loss factor (tan δ) of corresponding hydrogels calculated with storage and loss moduli. The bar plot data is represented in mean ± standard deviation. \*P < 0.05, \*\*P < 0.01, \*\*\*P < 0.001, n.s. no significant.

## 2.2. Characterization of hydrogels

Proton nuclear magnetic resonance ( $^1\text{H}$  NMR) and Fourier transform infrared (FTIR) spectrometry were performed to verify the composition and conjugation of AFG, AFG<sup>KLT</sup>, RFG, and RFG<sup>KLT</sup>. Hydrogels were lyophilized and grounded into powders. Powders of corresponding hydrogels were dissolved in deuterium oxide ( $\text{D}_2\text{O}$ , Sigma-Aldrich, USA) to obtain 10 mg/mL solution for  $^1\text{H}$  NMR. The 600M NMR spectrometer (JNM-ECA600, JEOL Ltd., Japan) was used to record the  $^1\text{H}$  NMR spectra at an ambient temperature. FTIR spectra of corresponding hydrogels were recorded with an FTIR spectrometer (X70, NETZSCH, Germany) using KBr pellets from 4000 to  $400\text{ cm}^{-1}$ .

For hydrogel morphology observation, AFG, AFG<sup>KLT</sup>, RFG, and RFG<sup>KLT</sup> dehydrated in successive concentrations of ethanol series (75 %, 80 %, 85 %, 90 %, 95 %, and 100 %; v/v), subjected to a  $\text{CO}_2$  critical point dryer (Samdri-PVT-3D, Tousimis, Rockville, MD, USA), and sputter-coated with 10 nm of platinum. The morphology of hydrogels was characterized by scanning electron microscopy (SEM, Carl Zeiss, GEMINISEM 500, Germany). To investigate transversal morphology, hydrogels were further observed with a transmission electron microscope (TEM, TECNAI Spirit, FEI, Czech Republic). Hydrogel samples were fixed with 2.5 % (v/v) glutaraldehyde for 3 h and 1 % osmium tetroxide solution for 1 h successively. Hydrogels were dehydrated, embedded in Epon 812 epoxy resin (Fluka, Münster, Germany), and cut into 70-nm-thick transverse ultrathin sections, followed by uranyl acetate staining for TEM imaging.

The binding and releasing rate of KLT peptides of AFG<sup>KLT</sup> and RFG<sup>KLT</sup> were assessed by HPLC (Agilent 1260, USA) assessment. The peptide solution before and after the immobilization process ( $n = 3$ ) was collected to assess the binding profile of KLT peptide on AFG and RFG. AFG<sup>KLT</sup> and RFG<sup>KLT</sup> ( $n = 3$ ) were soaked in PBS (pH = 7.4) at  $37^\circ\text{C}$  for 24 h, and the supernatants were collected to evaluate the released peptide concentration.

OCA15Pro Optical contact angle tester (Dataphysics, German) was applied for the measurement of the water contact angle of the hydrogels at ambient atmosphere and temperature. The images of a single water drop made on the corresponding hydrogels were recorded and the contacted angles were analyzed. To measure the water content of the hydrogels, the weights before and after lyophilization were measured ( $n = 3$ ) and the water content was calculated with the following equation:

$$\text{Water content (\%)} = (\text{wet weight} - \text{dry weight}) / \text{initial wet weight}$$

For the degradation assessment, hydrogels ( $n = 3$ ) were lyophilized, and their initial weights ( $W_0$ ) were accurately measured. Subsequently, the hydrogels were immersed in PBS at  $37^\circ\text{C}$  with gentle shaking. At predetermined time intervals, the samples were rinsed three times with pure water and lyophilized again to monitor their weights over time ( $W_t$ ). The degradation ratio was calculated using the following equation:

$$\text{Degradation Ratio (\%)} = (W_0 - W_t) / W_0$$

Rheological properties of the hydrogels were tested using a rheometer (MCR302e, Anton Paar GmbH, Graz, Austria) with an 8 mm-diameter parallel plate at  $37^\circ\text{C}$ . Storage ( $G'$ ) and loss ( $G''$ ) modulus of the hydrogels ( $n = 3$ ) were measured with dynamic frequency sweep test (1 % strain, 0.1–10 Hz), and the loss factors of hydrogels were with the following equation:

$$\text{Loss factor } (\tan \delta) = \text{loss modulus} / \text{storage modulus}$$

## 2.3. Cell culture

The RAW264.7 macrophage, human umbilical vein endothelial cell (HUVEC), rat Schwann cell-96 (RSC-96), and mouse fibroblast L929 cell lines were purchased from the Cell Bank of the Chinese Academy of Sciences (Shanghai, China). RAW264.7 was cultured in Dulbecco's

Modified Eagle's Medium (DMEM, Pricella) with 10 % FBS and 1 % PS. RSC-96 was cultured in High-Glucose Dulbecco's Modified Eagle's Medium (high glucose, DMEM, Pricella) with 10 % FBS and 1 % PS. HUVEC was cultured in an endothelial culture medium (Pricella) with 5 % FBS, 1 % PS, and 1 % endothelial cell growth supplement. Finally, L929 was cultured in Minimum Essential Medium (MEM, Pricella) with 10 % FBS and 1 % PS. All cells were cultured in an incubator containing 5 %  $\text{CO}_2$  at  $37^\circ\text{C}$ , and the fresh medium was changed every two days.

To evaluate the biological function of different hydrogels, RAW264.7, HUVEC, RSC-96, and L929 cells were directly seeded on RFG, RFG<sup>KLT</sup>, AFG, and AFG<sup>KLT</sup> hydrogels in 12 well culture plates. The blank control group was established by seeding the cells on a tissue culture plate (TCP). RAW264.7 macrophages were seeded on TCP or corresponding hydrogels at a density of  $4 \times 10^4$  cells/well, cultured in DMEM/F12 medium with or without  $1\ \mu\text{g/mL}$  lipopolysaccharide (LPS, Invitrogen, UK) and  $20\ \text{ng/mL}$  interferon- $\gamma$  (IFN- $\gamma$ , Abcam, UK), and performed various *in vitro* assessment after 24 h incubation. HUVEC, RSC-96, and L929 cells were seeded at a density of  $2 \times 10^4$  cells/well, and cultured on TCP or hydrogels in the correspondent medium for preset time, respectively, for further *in vitro* studies.

## 2.4. Live/dead staining in vitro

To evaluate cell compatibility of the hydrogels, HUVEC, RAW 264.7, RSC-96, and L929 cells were cultured on different hydrogels or TCP, respectively, and cultured for 24 h. Cells were then incubated with Calcein AM ( $2\ \mu\text{M}$ ) for 20 min, rinsed with PBS three times, and incubated with propidium iodide (PI) ( $2\ \mu\text{M}$ ) for 10 min further, and washed with PBS three times once more. After rinsing with PBS three times, the Live/Dead staining images were photographed with scanning confocal laser microscopy (Zeiss, Airyscan2-LSM980, Germany).

## 2.5. Quantitative reverse transcription polymerase chain reaction (qRT-PCR) in vitro

To evaluate gene expression of HUVEC, RAW264.7, RSC-96, and L929 cells on different hydrogels, qRT-PCR was carried out after the preset culture period. The total RNA of cells cultured on TCP, RFG, RFG<sup>KLT</sup>, AFG, or AFG<sup>KLT</sup> ( $n = 3$ ) was extracted with the RNAsimple Total RNA Kit (Tiangen, China), and the reverse transcription of cDNA was realized with FastKing RT kit (Tiangen, China). Subsequently, with the addition of SYBR Green supermix (Bio-Rad, USA), the qRT-PCR assessment was performed by a CFX96 real-time PCR detection system (Bio-Rad, USA). The relative gene expressions were normalized with the housekeeping gene, GAPDH, followed by the analysis carried out in  $2^{-\Delta\Delta\text{Ct}}$  method.

The primer sequences of target genes used in qRT-PCR are presented in Table S1.

## 2.6. Immunofluorescence staining in vitro

For *in vitro* immunofluorescence staining, HUVEC, RAW264.7, RSC-96, and L929 cells were cultured on different hydrogels or TCP, respectively, as previously described. Cells on hydrogels or TCP ( $n = 3$ ) were performed with the fixation in 4 % paraformaldehyde (PFA) for 1 h at  $4^\circ\text{C}$  after the preset culture period. Then, the samples were permeabilized in 0.1 % Triton X-100 (Sigma, USA) for 5 min, and blocked with 10 % normal goat serum (Solarbio, China) for 30 min. After incubation in primary antibody solutions overnight at  $4^\circ\text{C}$ , the samples were rinsed with PBS three times and immersed in secondary antibodies and DAPI (sc-74421, Santa Cruz, USA) for 1 h at room temperature in the dark. The immunofluorescence staining images were photographed with scanning confocal laser microscopy, and quantification analysis was performed with ImageJ 1.51k (Wayne Rasband, NIH, USA).

### 2.7. Enzyme-linked immunosorbent assay *in vitro*

The secretion capability of RAW264.7, HUVEC, and RSC-96 cells on different hydrogels was determined via enzyme-linked immunosorbent assay (ELISA). The supernatants of RAW264.7, HUVEC, and RSC-96 cultured on TCP or corresponding hydrogels were collected respectively. ELISA evaluation was performed with corresponding ELISA kits (Meimian, China) in accordance with the manufacturer's protocol. Finally, a microplate reader (EnSpire, PerkinElmer, USA) was used to measure the absorbance value at 450 nm.

### 2.8. Cell morphology assessment *in vitro*

The morphology of HUVEC cells on different hydrogels was observed with SEM. HUVEC cells cultured on TCP or different hydrogels ( $n = 3$ ) were fixed with 2.5 % glutaraldehyde for 2 h after three days of cultivation. Then, samples were dehydrated with consecutive ethanol rinse, dried with a CO<sub>2</sub> critical point dryer (tousimis, USA), and sputtered with 10 nm platinum film-coating. Finally, the samples were observed with field emission scanning electron microscopy (SEM, CarlZeiss, Oberkochen, Germany).

To observe the cellular morphology of L929 fibroblasts on different hydrogels, cytoskeleton staining was applied. L929 cells were cultured on TCP or different hydrogels ( $n = 5$ ), fixed in 4 % PFA for 30 min, permeabilized in 0.1 % Triton X-100 for 5 min, blocked in 10 % normal goat serum for 30 min, and incubated in Rhodamine Phalloidin (RP, Solarbio, China) for 2 h in dark successively. After staining the nuclei with DAPI for 40 min in the dark, the images of fibroblast morphology were captured with scanning confocal laser microscopy (LSM980 Airyscan2, Zeiss, Germany). Twenty-five cells were randomly taken for each sample, and the branching length of the fibroblasts was statistically analyzed with ImageJ 1.51k (Wayne Rasband, NIH, USA).

### 2.9. Transwell experiments *in vitro*

The recruitment capability of KLT peptides was evaluated by transwell experiments. RFG, RFG<sup>KLT</sup>, AFG, and AFG<sup>KLT</sup> hydrogels ( $n = 3$ ) were prepared on the lower chamber of 24-well culture plates. The 8.0 μm pore inserts (Labelect, China) were used as the upper chamber, and HUVEC cells were seeded at  $5 \times 10^3$  cells/well density on the inserts. The medium was added to the lower chamber, with the blank well as a control group. After 24 h cultivation, the inserts were collected, and the recruited HUVEC cells were fixed in 4 % PFA for 30 min, followed by 1 % (w/v) crystal violet staining for 10 min the images of recruited HUVEC cells were captured with an inverted microscope, and three images were taken randomly for each insert sample. The number of recruited HUVEC cells was counted for each image for the quantification analysis.

The effect of different hydrogels on cell migration profiles was investigated with a scratch wound healing assessment. L929 cells were seeded on the 24-well culture plate at a density of  $3 \times 10^4$  cells/well until the cell confluence reached approximately 90 %. Subsequently, a sterile 200 μL pipet tip was used to produce a straight scratch wound on the lower chamber for each well. The 0.4 μm pore inserts (Labelect, China) were inserted, and the upper chamber was filled with RFG, RFG<sup>KLT</sup>, AFG, or AFG<sup>KLT</sup> hydrogels respectively, including the empty inserts as the control group. The scratches on the lower chamber were photographed at 0 h and 24 h using an inverted microscope. The wound closure was measured and analyzed with ImageJ 1.51k (Wayne Rasband, NIH, USA).

### 2.10. Indirect co-culture assessment *in vitro*

The indirect coculture models were constructed to evaluate the regulation of different hydrogels on the interactions between different functional cells. RAW264.7, HUVEC, or RSC-96 cells were cultured on TCP, RFG, RFG<sup>KLT</sup>, AFG, and AFG<sup>KLT</sup> hydrogels ( $n = 3$ ) respectively for

the preset period. Then, the supernatants were collected, centrifuged, and preserved for further use. HUVEC, RSC-96, or L929 cells were seeded at a density of  $3 \times 10^4$  on the 12-well culture plate ( $n = 3$ ), and cultured for 72 h in a solution of the serum collected from the cell-hydrogel cultivation mixing with the fresh correspondent medium (1:1 v/v). The cells were finally collected and qRT-PCR, immunofluorescence staining, cytoskeleton staining, transwell experiments, and bright field photographs were performed as previously described for further analysis.

### 2.11. Animal procedures

Animal experiments of this study were performed in strict accordance with the Guide for Care and Use of Laboratory Animals of the National Institutes of Health, and all animal procedures were evaluated and granted by the Institutional Animal Care and Use Committee of Tsinghua University (Beijing, China, approval number: 22-WXM3). Healthy male SD rats (200–220 g,  $n = 60$ ) were used in the animal experiments. A diabetic rat model was introduced using intraperitoneal injection of premade streptozotocin (STZ, Sigma-Aldrich, USA) solution at a dose of 60 mg/kg, and considered as successfully established if the blood glucose level of the rat was above 16.7 mmol/L one week after the injection. Then, a full-thickness round-shaped skin wound (2 cm diameter) was created on the upper back of the rat after anesthetized with the combination of Zoletil and Xylazine (1 mL/kg) via intraperitoneal injection. Afterward, animals were randomly divided into five groups according to different wound treatments. The 2 cm-diameter round RFG, RFG<sup>KLT</sup>, AFG, and AFG<sup>KLT</sup> hydrogels were applied to fill and cover the wounds, while the control group was treated with saline solution. The wounds were photographed 7,14,21 and 28 days post-surgery, and wound areas were measured by Image Pro Plus 6.0 (Media Cybernetics, Silver Spring, USA) software.

### 2.12. Histological assessment

Rats were sacrificed at day 7, day 14, and day 28 post-surgery, and regenerated skin tissue samples from the wound area were collected the harvested tissue samples were fixed with 4 % (w/v) paraformaldehyde for 48 h, embedded in optimal cutting temperature compound (OCT, Tissue-Tek OCT Compound, USA), and sliced into 10 μm-thick histologic sections using a cryostat microtome (CM 1950, Leica, Germany). The tissue sections were further prepared for standard hematoxylin and eosin (H&E) staining, Masson staining, and immunofluorescence staining. H&E or Masson staining sections were observed with a Panoramic SCAN scanner (3DHIESTECH, Hungary) and processed using CaseCenter 2.9SP1 software (3DHIESTECH, Hungary).

For immunofluorescence staining, tissue sections were rinsed with PBS in advance. Subsequently, tissue sections were soaked in 0.3 % (w/v) Triton X-100 and 10 % (w/v) normal goat serum for 2 h and 4 h respectively at room temperature. Then, tissue sections were incubated with primary antibodies overnight at 4 °C. After rinsing with PBS, tissue sections were treated with secondary antibodies for 1 h, and DAPI (Abcam, UK) mounting medium for 20 min. Zeiss Axio Scan Z1 scanner (Carl Zeiss, Germany) was used to capture immunofluorescence staining images, Zen 2.6 (Blue edition) software (Carl Zeiss, Germany) was used for further image processing, and ImageJ 1.51 k (Wayne Rasband, NIH, USA) was used for quantitative analysis.

The primary and secondary antibodies used in histological staining are listed in Table S2.

### 2.13. Statistical analysis

All data is presented in mean ± standard deviation and statistically analyzed with the SPSS Statistics for Windows (v.23.0; IBM Corp., USA). The statistical differences between multiple comparisons were determined by one-way factorial analysis of variance (ANOVA), followed by

LSD post hoc test for equal variances, or Dunnett's T3 post hoc test for unequal variances. All tests in this study were conducted two-sided, and statistical significance was considered with \* $P < 0.05$ , \*\* $P < 0.01$ , and \*\*\* $P < 0.001$ .

### 3. Results and discussion

#### 3.1. Fabrication and characterization of AFG<sup>KLT</sup> hydrogel

The AFG hydrogels were fabricated via electrospinning as reported previously [40]. The angiogenic peptide, RAD/KLT (Ac-(RA-DA)<sub>4</sub>-G<sub>4</sub>-KLTWQELYQLKYKGI-CONH<sub>2</sub>) was applied to functionalize AFG in an interpenetrating network manner by molecular self-assembly to generate aligned bioactive nanofiber hydrogel. The RAD/KLT peptides infiltrated into the interstitial space of the aligned fibrin nanofibers network and underwent self-assembly into thin nanofibers that were further stabilized by EDC/NHS crosslinking. For comparison, random fibrin hydrogel (RFG) and its composite counterpart RFG<sup>KLT</sup> were also fabricated via direct enzymatic gelation. The successful fabrication of various hydrogels was evaluated with <sup>1</sup>H NMR and FTIR spectrum. In the <sup>1</sup>H NMR spectra, fibrinogen showed a strong peak at 3.48 ppm, while AFG<sup>KLT</sup> showed a down-shifted peak at 3.62 ppm, indicating the molecular interactions between peptides and fibrin network (Fig. 1B). Meanwhile, two strong absorption peaks at 3075 cm<sup>-1</sup> and 3290 cm<sup>-1</sup> were observed in both KLT peptide and AFG<sup>KLT</sup>, which was ascribed to the typical N-H stretching for peptides, while fibrinogen exhibited only one absorption peak at 3290 cm<sup>-1</sup> (Fig. 1C). These results were consistent with previous studies [41], confirming the successful fabrication of AFG<sup>KLT</sup> hydrogels. Further, no obvious distinction was detected in <sup>1</sup>H NMR and FTIR spectrum between RFG and AFG or RFG<sup>KLT</sup> and AFG<sup>KLT</sup> (Fig. S1, Supporting Information), confirming that the chemical structure of fibrinogen remains intact during electrospinning, whereas the bioactive functionalization in both aligned or random hydrogels was carried out in an identical conjugation.

The AFG hydrogel, fabricated via electrospinning, exhibited a white, opaque, anisotropic fiber-bundle structure, whereas the RFG hydrogel formed as a white, bulk-like gel. After modification with interpenetrating self-assembling peptides, both AFG<sup>KLT</sup> and RFG<sup>KLT</sup> became relatively transparent because of increased water content while retaining their respective macroscopic configurations (Fig. S2, Supporting Information). The microstructure of the hydrogels was observed using SEM imaging (Fig. 1D). Unlike the randomly distributed fibrous structure that was observed in RFG and RFG<sup>KLT</sup>, highly oriented nanofibers with around 100 nm in diameter were visualized in AFG and AFG<sup>KLT</sup>, reflecting the successful fabrication of anisotropic structures in nanoscale via electrospinning. Also, AFG<sup>KLT</sup> and RFG<sup>KLT</sup> exhibited tiny self-assembling peptide nanofibers (10–20 nm in diameter) uniformly covering the fibrin nanofibers, indicating that the fibrin system did not disrupt the self-assembling process. TEM images manifested the cross-sectional microstructure of nanofibers in four different hydrogels (Fig. 1E). Transactions of fibers in AFG and AFG<sup>KLT</sup> hydrogels showed identical circular shapes compared to the nonuniform transactions shape of RFG and RFG<sup>KLT</sup>. Moreover, AFG<sup>KLT</sup> exhibited a visibly larger diameter of fibers than AFG. The increase in fiber diameter was attributed to the conjugation of self-assembling peptides and their hydrophilic feature. The morphologies also confirmed that the self-assembling peptides could penetrate the fibrin fiber interior to remodel the morphology thoroughly.

Further, the binding and release profiles of the bioactive peptides were examined. The RAD/KLT peptides showed a significantly higher binding rate in AFG<sup>KLT</sup> (84.9 ± 1.2 %) than in RFG<sup>KLT</sup> (79.5 ± 1.0 %) (Fig. 1F). Moreover, a higher peptide-releasing rate was observed in AFG<sup>KLT</sup> in comparison to RFG<sup>KLT</sup> after 7 days in PBS at 37 °C (Fig. 1G). The aligned nanofibrous structure of AFG hydrogels endowed them with lower resistance to molecular diffusion inward or outward compared to random nanofibrous hydrogels. The peptides RAD/KLT were much

easier to infiltrate and release out of AFG, thus contributing to a higher peptide-binding rate and releasing rate. Simultaneously, the AFG<sup>KLT</sup> and RFG<sup>KLT</sup> showed significantly smaller contact angles in comparison to AFG and RFG respectively, indicating the hydrophilicity of fibrin hydrogel was enhanced by peptide immobilization (Fig. 1H). This improved hydrophilicity facilitates better cell adhesion, which is critical for guiding cellular behaviors such as cytoskeletal alignment and directional growth [42]. Furthermore, the AFG<sup>KLT</sup> exhibited the highest water content among the hydrogels, attributed to the combined effects of its aligned structure and the presence of hydrophilic peptides (Fig. 1I), helping to maintain a moist wound environment and to promote an optimal microenvironment for active cellular responses and interactions [43]. Additionally, the degradation profile of the hydrogels was evaluated. As shown in Fig. S3 (Supporting Information), the degradation profiles of the four hydrogels showed no significant differences, with noticeable degradation occurring within two weeks.

The viscoelasticity properties of hydrogels were then evaluated with rheological measurements. As shown in Fig. 1J, in the frequency sweep from 0.1 to 10 Hz at a constant 1 % deformation, hydrogels exhibited relatively stable storage modulus ( $G'$ ) and loss modulus ( $G''$ ), demonstrating fibrin hydrogels could provide steady structural support within such range of shear stress. The average  $G'$  and  $G''$  values of AFG<sup>KLT</sup> hydrogel were significantly higher than those of AFG hydrogel (Fig. 1K). This increase in elasticity and viscosity in the AFG<sup>KLT</sup> hydrogel is likely attributable to the chemical crosslinking process involving EDC/NHS, which enhances the chemical bonding between the fibrin network and the self-assembled peptides. Such modifications improved the viscoelastic properties of the hydrogel, making it more suitable for applications in skin tissue regeneration. Additionally, the average loss factor ( $\tan\delta$ ) of the hydrogels closely aligns with the viscoelastic properties of soft tissues ( $\tan\delta \sim 0.1\text{--}0.2$ ) (Fig. 1L) [44].

To assess cytocompatibility, four representative cell types (HUVEC, RAW 264.7, RSC-96, and L929) were cultured on the RFG, RFG<sup>KLT</sup>, AFG, and AFG<sup>KLT</sup> hydrogels. As illustrated in Fig. S4 (Supporting Information), all cell types exhibited high survival rates across these hydrogels, with negligible differences compared to the TCP control group. These findings demonstrate the excellent biocompatibility of fibrin-based hydrogels and also imply that the electrospinning fabrication process does not introduce additional safety concerns.

Furthermore, it is well-established that the modulation upon multiple cell behaviors can be achieved through structural guidance via facilitating mechanosensing and mechanotransduction [45–47]. Meanwhile, activation of VEGF signaling pathway can also contribute to promoting various cellular processes, notably secretion capabilities, in different cell types [48–52]. Based on the features of oriented fibrous structure and pro-angiogenic functionalization, we propose that the designed bioactive anisotropic hydrogels have great potential for modulating multiple cell behaviors. Therefore, we investigated the gene expression levels of key markers in the four cell types. Results showed significant upregulation of integrin and focal adhesion kinase (FAK) in cells cultured on anisotropic hydrogels (AFG and AFG<sup>KLT</sup>), highlighting enhanced mechanosensing and mechanotransduction driven by the oriented fibrous structures (Fig. S5, Supporting Information). Additionally, the expression of VEGF receptor (VEGFR) was markedly elevated in the RFG<sup>KLT</sup> and AFG<sup>KLT</sup> groups among four cell types, demonstrating the notable bioactive effects of KLT (Fig. S6, Supporting Information). This indicated that the VEGF-mimicking motifs might facilitate various cellular behaviors, such as secretion, further enhancing multicellular interactions.

Collectively, in this study, we systematically evaluated the multicellular modulation capabilities of anisotropic bioactive hydrogels *in vitro* by examining their effects on key cellular processes and enhanced intercellular crosstalk among endothelial cells, macrophages, Schwann cells, and fibroblasts, to further validate their regenerative potential and the effectiveness of our novel strategy for diabetic wound healing.

### 3.2. AFG<sup>KLT</sup> hydrogel induced vascularization of endothelial cell *in vitro*

Angiogenesis is one of the most crucial factors in diabetic wound healing, for alleviating hypoxia and ischemia [53]. The pro-angiogenic effect of the hydrogels was determined with HUVECs *in vitro*. The transwell migration assay revealed that a significantly higher number of HUVECs migrated through the membrane in AFG<sup>KLT</sup> and RFG<sup>KLT</sup> in comparison to the non-functionalized counterpart (Fig. 2A and C), indicating the functionalization with VEGF-mimic peptide enhanced the migration and recruitment of HUVECs. Meanwhile, the number of recruited cells in the AFG<sup>KLT</sup> group ( $210 \pm 16$  cells/field) was significantly larger than RFG<sup>KLT</sup> group ( $174 \pm 10$  cells/field), but no significance was found between the AFG group ( $96 \pm 10$  cells/field) and RFG group ( $96 \pm 10$  cells/field). This result demonstrated the structural orientation of fibrous hydrogels does not affect cell behavior in the absence of physical attachment between the cell and matrix. However, the higher peptide-releasing efficiency induced by the oriented fibers can indirectly promote endothelial cell recruitment through enhanced bioactivity presentation.

The vascularization of endothelial cells is closely linked to their

morphogenesis [54]. To elucidate the impacts of physical and bioactive cues of AFG<sup>KLT</sup> on HUVEC morphogenesis, we observed CD31 (Platelet endothelial cell adhesion molecule-1, PECAM-1/CD31) expression after one day of culture. As depicted in Fig. 2B, HUVECs on AFG and AFG<sup>KLT</sup> hydrogels showed aligned CD31 expression parallel to the fiber direction, in contrast to the RFG and RFG<sup>KLT</sup> groups. Moreover, in the AFG<sup>KLT</sup> group, CD31 expression of HUVECs extended into the fiber matrix, forming abundant overlapping connections with neighboring cells and exhibiting longer cytoskeletal extensions. Immunostaining images revealed that endothelial cells could sense the oriented physical signals and pro-angiogenic bioactive signals with cell adhesion molecules, responding with dominant morphogenesis activation along the fiber direction and enhanced intercellular connections. Additionally, SEM images of HUVECs on AFG<sup>KLT</sup> and RFG<sup>KLT</sup> hydrogels exhibited tube-like assemblies, indicating the bioactive motifs of KLT peptides significantly enhanced the morphological differentiation of endothelial cells with more cellular protrusions, while oriented and randomly distributed morphology were observed in AFG and RFG groups, respectively (Fig. 2D). Also, the relatively larger capillary-like structure formation in AFG<sup>KLT</sup> compared to the RFG<sup>KLT</sup> group suggested a synergistic effect of

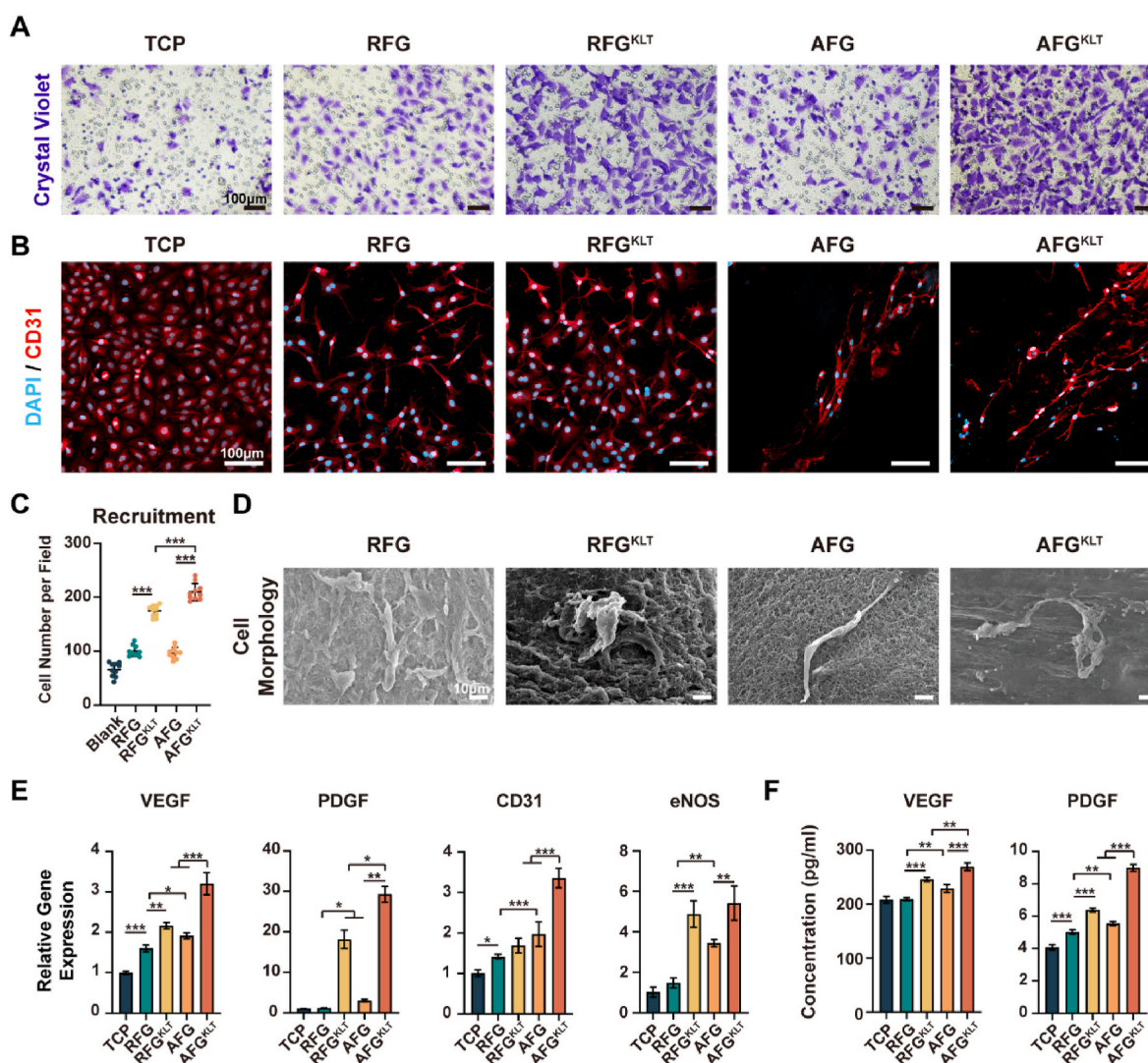


**Fig. 2.** AFG<sup>KLT</sup> hydrogel induced morphological differentiation and organization of endothelial cells. A) Representative photographs of the HUVEC recruitment in different groups at 24 h. B) Representative immunostaining images of HUVECs with CD31 (red) and DAPI (blue) cultured on different hydrogels for 24 h. C) Quantification analysis of the recruited HUVECs number per field. D) Representative SEM images of HUVECs cultured on different hydrogels for 24 h. E) Relative gene expression of HUVECs cultured on different hydrogels for 72 h. F) The secretion of VEGF and PDGF of HUVECs cultured on different hydrogels for 72 h. The bar plot data is represented in mean  $\pm$  standard deviation. \* $P < 0.05$ , \*\* $P < 0.01$ , \*\*\* $P < 0.001$ , n.s. no significant.

aligned fiber topography and pro-angiogenic peptide on vascularization. Collectively, the above results indicated that RAD/KLT peptide could significantly activate cell morphogenesis and accelerate the tubulogenesis of endothelial cells, and the fibrous orientation, as a physical cue, guided cytoskeletal reorganization of HUVECs and enhanced responses to pro-angiogenic bioactive cues.

To further investigate the angiogenesis-inducing activity of the AFG<sup>KLT</sup> hydrogel, we carried out qRT-PCR and ELISA assessments to evaluate the angiogenic behavior at the genetic expression and secretion levels in HUVECs cultured on different hydrogels for three days. VEGF and PDGF (Platelet-derived growth factor) are two crucial growth factors essential for blood vessel formation [55]. The genetic expression of VEGF and PDGF was significantly upregulated (Fig. 2E), and the secretion levels of these cytokines were the highest in the AFG<sup>KLT</sup> groups (Fig. 2F). Similarly, the RFG<sup>KLT</sup> groups were comparably higher than the RFG group, respectively in both genetic and secretion expression. These results manifested that the pro-angiogenic KLT peptides have a dominant effect on angiogenesis by facilitating the expression of VEGF and PDGF. Moreover, the expression levels of VEGF and PDGF in the AFG and AFG<sup>KLT</sup> groups were relatively higher than the RFG and RFG<sup>KLT</sup> groups, respectively, suggesting that structural alignment offered larger cell extension guidance, potentially leading to higher availability for cell-matrix interaction. Additionally, the genetic expression of CD31 was significantly higher in the aligned fibrin hydrogels (AFG and AFG<sup>KLT</sup>) groups in comparison to the random fibrin hydrogels (RFG and RFG<sup>KLT</sup>), demonstrating the angiogenic activities in HUVECs were better activated by the topographical cues of fibrous orientation (Fig. 2E). The significantly upregulated expression in the AFG<sup>KLT</sup> group compared with the AFG group indicated the KLT peptide could provide the VEGF-mimetic motifs, for further enhancing vascularization. Furthermore, HUVECs in the AFG<sup>KLT</sup> group exhibited a comparably higher gene expression level of eNOS (endothelial nitric oxide synthase), indicating the reduced cellular apoptosis and enhanced vascularization [56]. Also, the AFG<sup>KLT</sup> group presented the highest level of HIF- $\alpha$  (Hypoxia-inducible factors- $\alpha$ ), and FGF-2 (Fibroblasts growth factor-2) expression (Fig. S7, Supporting Information), suggesting that AFG<sup>KLT</sup> hydrogel might elevate hypoxic-induced activation sensitivity and enhance pro-regenerative factors secretion in endothelial cells, which could promote the optimization of vascular microenvironment.

### 3.3. AFG<sup>KLT</sup> hydrogel regulated anti-inflammatory polarization of macrophages *in vitro*

The inflammation phase in the wound healing procedure is mainly carried out by macrophages, via clearing the wounded tissue, enhancing host defense, and assisting the phase transition towards tissue regeneration [57–59]. The impaired phenotypic switch of macrophages from M1 to M2 in diabetic wounds is responsible for the destructive microenvironment and chronic wound establishment [60]. In recent studies, the topological structures are verified to contribute to macrophage phenotypic transition [61], for example, the aligned fibrous structures are capable of inducing macrophage polarization towards M2 phenotype via cytoskeletal guidance [62].

To investigate the anti-inflammatory regulation of AFG<sup>KLT</sup> hydrogel, we conducted the immunostaining, qRT-PCR, and ELISA evaluations with RAW 264.7 macrophages culturing on different hydrogels for 24 h. To better simulate the pro-inflammatory presence in diabetic wound sites, RAW 264.7 cells were pre-treated with lipopolysaccharide (LPS) and interferon- $\gamma$  (IFN- $\gamma$ ) for 12 h to classically activate toward the M1 phenotype in TCP (served as control group) and corresponding hydrogel groups [63]. The non-treated groups were also established to serve as blank group, where cells were kept in the static states without polarization.

Immunofluorescent staining was performed to visualize the phenotypic expression of macrophages. As depicted in Fig. 3A and B, the AFG and AFG<sup>KLT</sup> groups showed lower iNOS (M1 marker) and higher CD206

(M2 marker) positive expression compared to the TCP group (classically activated as M1 phenotype without hydrogel treatment), reflecting the anti-inflammatory effect of aligned fiber structures. Further, to quantify the macrophage polarization into M1 or M2 phenotypes, we evaluated the proportion of iNOS-positive cells (Fig. 3C) or CD206-positive cells (Fig. 3D) among CD68-positive cells (total activated macrophage marker). In comparison with the non-treated group, the iNOS+/CD68+ cell ratio in the TCP groups was prominently higher ( $97.25 \pm 1.26\%$ ), while the CD206+/CD68+ ratio was significantly lower ( $4.19 \pm 0.86\%$ ), confirming the successful induction towards M1 pro-inflammatory phenotype with dual stimulation of LPS and IFN- $\gamma$  in TCP and hydrogel groups. The AFG and AFG<sup>KLT</sup> groups present a significantly lower iNOS positive ratio than the RFG and RFG<sup>KLT</sup> groups, respectively. Conversely, the proportion of macrophages with CD206 positive expression was significantly higher in the aligned fibrin hydrogels (AFG and AFG<sup>KLT</sup>) compared to random fibrin hydrogels (RFG and RFG<sup>KLT</sup>). These results manifested that the oriented physical signals prominently suppressed the M1 phenotype induction and promoted the M2 phenotype transition. It is well documented that M2 macrophages exhibit an elongated cellular morphology, while the M1 macrophages typically display a pancake-like shape [64]. The physical cues of oriented fibrous structures might provide guidance for cellular elongation and alignment, which could lead to shape-induced polarization of macrophages towards the M2 phenotype. Additionally, the AFG<sup>KLT</sup> group showed a stronger polarization regulation effect compared to the AFG group. Given that VEGF is a pro-regenerative cytokine secreted by M2 macrophages, it likely facilitates the phenotypic transition from M1 to M2, suggesting the VEGF-mimetic peptide may act as a bioactive cue in polarization regulation.

The immunoregulatory effects of AFG<sup>KLT</sup> hydrogel contribute to optimizing the anti-inflammatory microenvironment by modulating cytokine secretion and relative gene expression from macrophages. Interleukins are a group of cytokines, mainly secreted by immune cells, participating as a central role in immune responses and interactions. Especially, IL-6 (interleukin-6) is a typical pro-inflammatory cytokine promoting acute inflammation reactions [65], and IL-10 (interleukin-10) is a classical anti-inflammatory cytokine with pro-regenerative effects [66]. Our findings showed that macrophages cultured on AFG<sup>KLT</sup> or AFG hydrogels secreted significantly lower levels of IL-6 and higher levels of IL-10 compared to the RFGKLT and RFG groups (Fig. 3E and F). This result indicated that aligned topographical structures can reduce the secretion of pro-inflammatory factors while increasing the secretion of anti-inflammatory factors, thereby improving the immune microenvironment to support tissue regeneration. Moreover, genetic expression was assessed via qRT-PCR. The expression levels of M1 phenotypic genes, including TNF- $\alpha$  (tumor necrosis factor- $\alpha$ ), iNOS, IL-6, CD86, and IL-1 $\beta$  were significantly downregulated in the AFG<sup>KLT</sup> and AFG groups (Fig. 3G and Fig. S8, Supporting Information). In contrast, the AFG<sup>KLT</sup> hydrogel notably upregulated the expression of M2 macrophage markers, such as Arg-1 (arginase-1), CD206, IL-10, Fizz, YM-1, and VEGF (Fig. 3H and Fig. S8, Supporting Information). It is also noteworthy that VEGF expression was significantly increased in both the AFG<sup>KLT</sup> and RFG<sup>KLT</sup> groups compared to the AFG and RFG groups, respectively. This suggested that the KLT peptide may participate in macrophage regulation as a bioactive signal, by promoting the expression of VEGF, an anti-inflammatory factor.

### 3.4. AFG<sup>KLT</sup> hydrogel promoted schwann cell maturation *in vitro*

Recent studies highlighted the crucial role of Schwann cells in chronic wound healing [67–69]. Along with Schwann cell maturation, they exhibit significantly enhanced myelination and neurotrophic secretion capabilities, providing neuronal support for regenerated nerves and optimizing the neural microenvironment with neurotrophins and various growth factors. This process accelerates skin tissue regeneration and alleviates diabetic wound neuropathy [70]. To investigate



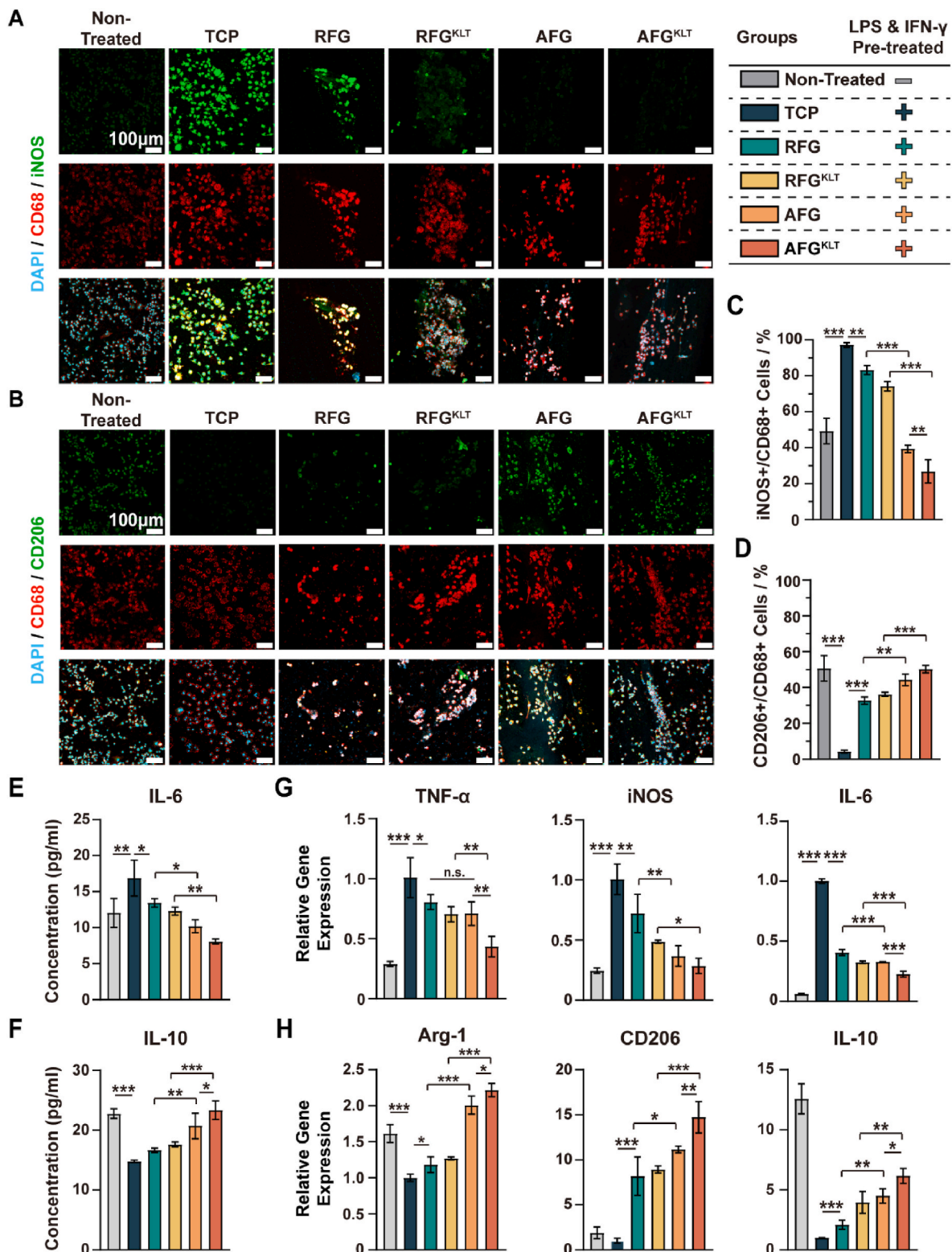


**Fig. 3.** AFG<sup>KLT</sup> hydrogel regulated anti-inflammatory polarization of macrophages. A) Representative immunostaining images of RAW 264.7 macrophages with iNOS (green), CD68 (red), and DAPI (blue) cultured on different hydrogels and conditions for 24 h. B) Representative immunostaining images of RAW 264.7 macrophages with CD206 (green), CD68 (red), and DAPI (blue) cultured on different hydrogels and conditions for 24 h. C, D) Quantification analysis of the percentage of iNOS-positive (C) and CD206-positive (D) cells over CD68-positive cells. E, F) The secretion of IL-6 (E) and IL-10 (F) of RAW 264.7 macrophages cultured on different hydrogels and conditions for 24 h. G, H) Relative pro-inflammatory (G) and anti-inflammatory (H) gene expression of RAW 264.7 macrophages cultured on different hydrogels and conditions for 24 h. The bar plot data is represented in mean  $\pm$  standard deviation. \*P < 0.05, \*\*P < 0.01, \*\*\*P < 0.001, n.s. no significant.

the effect of physical and bioactive cues on Schwann cell maturation, we evaluated the genetic and protein-level expression of RSC-96 cells.

The maturation process of Schwann cells into myelinating glial cells is promoted by the elongated morphological transition and unified cellular alignment [71]. Schwann cells cultivated on TCP or different hydrogels for three days were identified with S100 and p75 Schwann cells markers (Fig. 4A) [34]. Schwann cells showed a spreading cytoskeleton and formation of protuberance on different fibrin hydrogels, but exhibited more spherical morphology on TCP, revealing the promoted cell adhesion and morphogenesis of Schwann cells on fibrin hydrogels. In both AFG and AFG<sup>KLT</sup> groups, the cytoskeleton of Schwann cells showed highly oriented cytoskeletal alignment parallel to the fiber direction, while the random distribution of cytoskeleton was depicted in

the RFG and RFG<sup>KLT</sup> groups, demonstrating the enhanced cell orientation was induced by the fibrin fibers alignment for myelination. Further, the relative gene expression was examined by qRT-PCR after three-day cultivation to investigate the genetic modulation of bioactive aligned hydrogel on RSC-96 cells (Fig. 4B). The AFG hydrogel significantly upregulated the myelination-related gene expression, including S100, MBP (myelin basic protein), PMP22 (peripheral myelin protein), NRP2 (neuropilin-2), and P0 (myelin protein zero), compared to the RFG group. Further, the expression level of NCAM (Neuronal cellular adhesion molecules), highly expressed by immature Schwann cells [72], was prominently lower in the AFG groups than the RFG groups. These results indicated the fibrous physical cues could notably promote the expression of myelination, with effective enhancement in cellular alignment

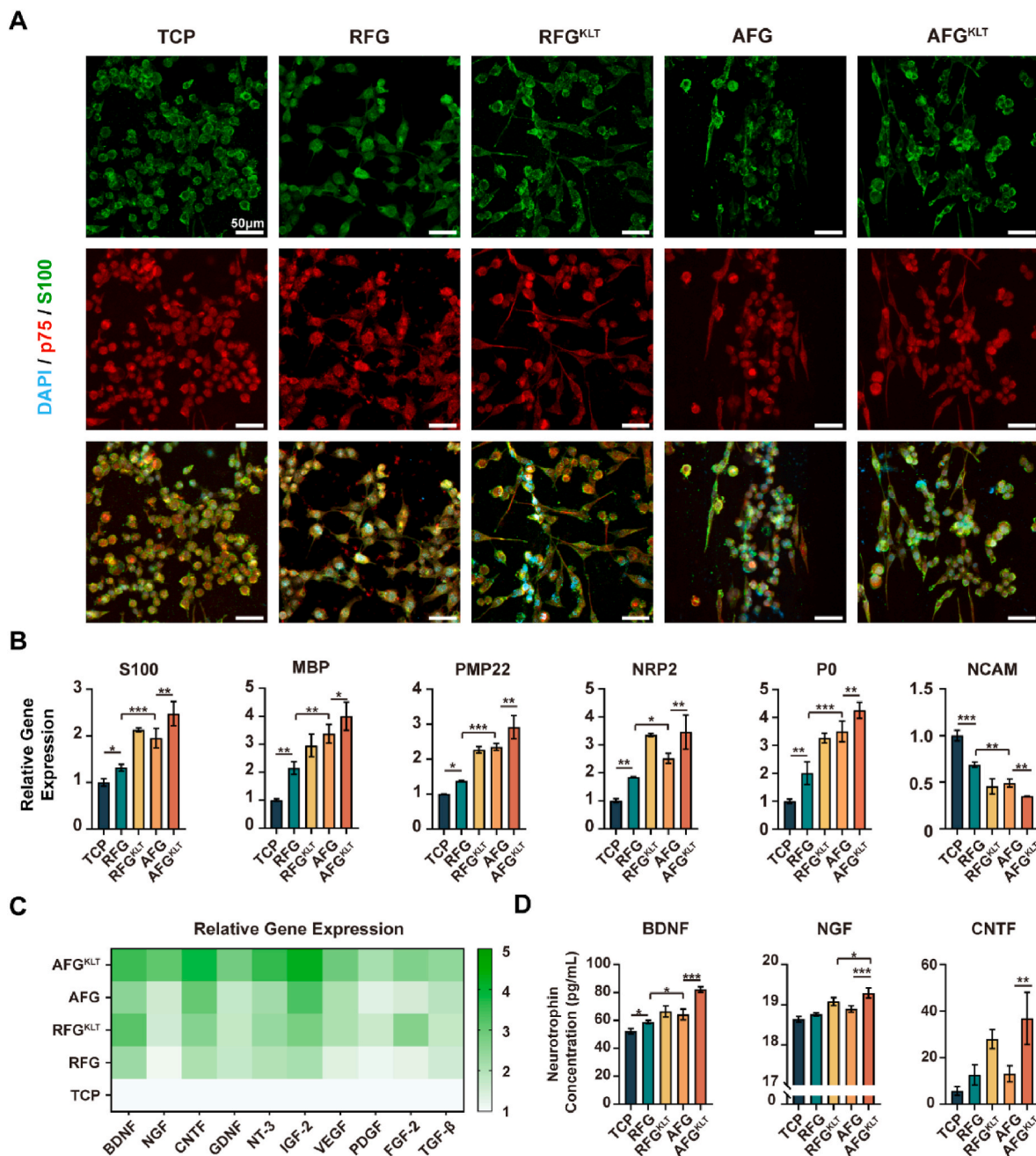


**Fig. 4.** AFG<sup>KLT</sup> hydrogel promoted Schwann cell maturation. A) Representative immunostaining images of RSC-96 with S100 (green), p75 (red), and DAPI (blue) cultured on different hydrogels for 72 h. B, C) Relative gene expression of maturation (B) and secretion (C) related genes cultured on different hydrogels for 72 h. D) The neurotrophin secretion of BDNF, NGF, and CNTF of RSC-96 cultured on different hydrogels for 72 h. The bar plot data is represented in mean ± standard deviation. \*P < 0.05, \*\*P < 0.01, \*\*\*P < 0.001, n.s. no significant.

and orderly organization. Meanwhile, the genetic expression in the AFG<sup>KLT</sup> group was also comparably upregulated, compared with the AFG group, suggesting that the bioactive peptide may positively influence Schwann cell maturation. This effect is likely due to the interlocking crosstalk between neurogenesis and angiogenesis, potentially guiding Schwann cell maturation with pro-angiogenic cues.

Schwann cells could also refine the neurogenic microenvironment through enhanced secretion of various neurotrophins and pro-regenerative growth factors [73]. We investigated the secretion-related genes from Schwann cells, including BDNF (brain-derived neurotrophic factor), NGF (nerve growth factor), CNTF (ciliary neurotrophic factor), GDNF (glial cell line-derived neurotrophic factor), NT-3 (Neurotrophin-3), IGF-2 (insulin-like growth factor-2), VEGF, PDGF, FGF-2, and transforming growth factor- $\beta$  (TGF- $\beta$ ). As shown in Fig. 4C, the heatmap of relative gene expression revealed that genetic expression was the strongest in the AFG<sup>KLT</sup> group, demonstrating the synergistic reinforcement of potential secretion capability with dual physical oriented and bioactive signals. In addition, we verified the secretion behavior with ELISA, detecting the secreted concentration of BDNF, NGF, and CNTF neurotrophins (Fig. 4D). The results showed a similar trend as genetic evaluation, presenting the highest level of neurotrophins secretion with notable significance in the AFG<sup>KLT</sup> group. These results reveal that, on one hand, the anisotropic fibrous structure can induce Schwann cell maturation and further enhance their secretion abilities. On the other hand, bioactive motifs that mimic growth factors could promote cytokine secretion. The synergistic effect of bioactive

aligned hydrogel leads to significantly enhanced neurotrophic factor secretion, which presents crucial development in neurotrophic micro-environment refinement, positively promoting neurogenesis in the diabetic wound sites. Moreover, the reinforced secretion of pro-regenerative factors, such as IGF-2, VEGF, and TGF- $\beta$ , suggested that modulation of Schwann cells could indirectly promote cellular proliferation, migration, vascularization of endothelial cells, and activation of fibroblasts, promoting multicellular crosstalk to facilitate multidimensional acceleration in diabetic wound healing and skin tissue regeneration [74].

### 3.5. AFG<sup>KLT</sup> hydrogel facilitated ECM remodeling capability of fibroblasts *in vitro*

Broadly, fibroblasts are regarded as the pivotal cells responsible for extracellular matrix (ECM) regeneration and deposition in the structural framework of skin tissues [75]. Fibroblasts migrate to the wound site under the stimuli of various cytokines, mechanical tension, and inter-cellular interactions to synthesize native-like ECM [76]. Especially in the remodeling phase of wound healing, functional fibroblasts are the key to healthy wound repair via consecutive crosslinking and rebuilding of ECM on the wound site [77]. To investigate the fibroblast behavior upon the influence of fibrin hydrogels, migration capability, cytoskeleton alignment, and remodeling-related expression were evaluated with L929 cells cultivated on different hydrogels for three days.

The migration capability of the fibroblasts was assessed with the

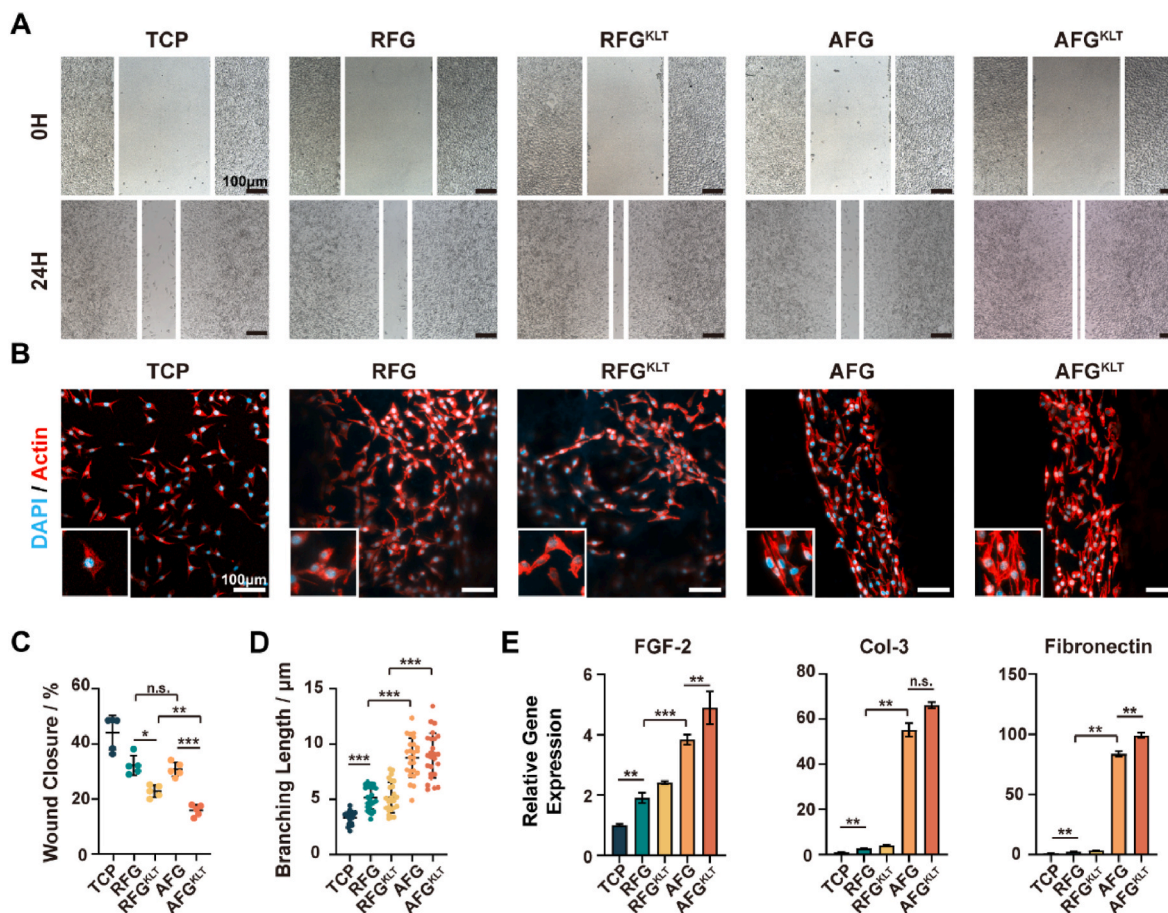


**Fig. 5.** AFG<sup>KLT</sup> hydrogel facilitated ECM remodeling capability of fibroblasts. A) Representative photographs of scratch wound healing assay of L929 fibroblasts in different groups at 0 h and 24 h. B) Representative cytoskeleton staining images of L929 fibroblasts cultured on different hydrogels for 72 h visualized by staining with phalloidin (red) and DAPI (blue). C) Quantification analysis of scratch wound closure at 24 h. D) Quantification analysis of L929 fibroblasts cytoskeleton branching lengths cultured on different hydrogels for 72 h. E) Relative gene expression of L929 fibroblasts cultured on different hydrogels for 72 h. The bar plot data is represented in mean  $\pm$  standard deviation. \* $P < 0.05$ , \*\* $P < 0.01$ , \*\*\* $P < 0.001$ , n.s. no significant.

scratch assay (Fig. 5A). Overall, the AFG<sup>KLT</sup> group exhibited a wound closure of  $15.86 \pm 2.04$  % and demonstrated the most rapid wound healing effect after 24 h (Fig. 5C). The wound closure was the slowest in the blank control group ( $44.11 \pm 6.17$  %) showing that fibrin components of the hydrogel had promoted migration throughout the degradation, functioning as the chemical cues for fibroblasts. As evidenced by the significant differences in wound closure between the AFG<sup>KLT</sup> and the AFG groups ( $30.80 \pm 2.55$  %), the self-assembled bioactive peptides might significantly enhance the migration capability of L929 cells, due to the existence of VEGF receptor in fibroblasts [78].

The cytoskeleton of L929 cells was stained with Phalloidin/DAPI for observation (Fig. 5B). The four hydrogel groups exhibited superior cell adhesion presenting sprouted and branching morphology of fibroblast in comparison with the TCP group, demonstrating the enhanced cellular adhesion with fibrin matrix components as the chemical cues. The randomly distributed cytoskeleton was visualized in the RFG and RFG<sup>KLT</sup> groups, while highly aligned cytoskeleton orientation was observed in the AFG and AFG<sup>KLT</sup> groups. The quantitative results showed that the AFG group ( $8.76 \pm 1.77$   $\mu$ m) and the AFG<sup>KLT</sup> group ( $8.96 \pm 2.03$   $\mu$ m) exhibited significantly longer cytoskeletal extension than the RFG group ( $5.13 \pm 1.03$   $\mu$ m) and the RFG<sup>KLT</sup> ( $5.18 \pm 1.38$   $\mu$ m), respectively (Fig. 5D), indicating that fibroblasts tended to form more aligned cell projection and elongated cytoskeleton induced by aligned fiber structure of fibrin hydrogels. Given the orderly organized characteristics of natural skin tissue, the fibroblasts' alignment might exhibit promising effects on skin tissue regeneration and functional recovery.

The primary functions of recruited fibroblasts at the wound site include growth factor secretion, ECM synthesis, and intercellular connection formation. During the regeneration and remodeling of wounded skin tissue, fibroblasts secrete cytokines, such as FGF-2, to optimize the pro-regenerative microenvironment [79]. Subsequently, fibroblasts synthesize and deposit ECM components, including collagen III and collagen I, to reconstruct the tissue framework [80]. Finally, intercellular binding proteins, such as fibronectin and laminin, are formed to establish stable intercellular connections [81]. Therefore, we investigated the representative functional gene expression of fibroblasts to elucidate the modulation by bioactive aligned hydrogels. As shown in Fig. 5E, the expression of FGF-2, Col-3 (collagen III), and fibronectin genes was significantly upregulated in the aligned fibrin hydrogel groups, demonstrating the effectiveness of the physical alignment signals provided to the fibroblasts. These cells were activated through mechanosensing and mechanotransduction of the physical signals presented by the aligned fibrin hydrogels, resulting in enhanced proliferation, migration, secretion, and intercellular interactions [82]. Additionally, it is worth noting that the AFG<sup>KLT</sup> group exhibited significantly higher expression in FGF-2 and fibronectin compared to the AFG group, suggesting that the enhanced bioactivity of hydrogels could positively facilitate cytokine secretion and cell-cell interactions. In contrast, no prominent differences were observed in the expression of Col-3 between the two groups, suggesting that ECM deposition is predominantly regulated by the oriented physical cues provided by the anisotropic hydrogel structure.

### 3.6. AFG<sup>KLT</sup> hydrogel modulated inter-microenvironmental crosstalks in vitro

Given that the impaired microenvironment in diabetic wounds results from the dysregulation of various cells and their complex interactions, merely modulating specific cell behaviors is insufficient for optimizing the microenvironment. Intercellular crosstalks that primarily consist of intercellular connections and indirect interactions via the paracrine effect play an important role in tissue regenerative repair [83]. Therefore, we utilized an indirect co-culturing model to evaluate the capacity of AFG<sup>KLT</sup> hydrogel in microenvironment refinement via modulating multicellular crosstalks. The facilitation of intercellular crosstalk mediated by different hydrogels was investigated by culturing

RAW 264.7, HUVEC, or RSC-96 cells on respective hydrogels, followed by culturing other cell types with the collected supernatant. The TCP groups represent the intercellular crosstalk without any hydrogel treatment, while the blank control was established to observe the natural cell behaviors without interference from interactions between cells (Fig. 6 and Figs. S9–S11, Supporting Information).

Initially, we evaluated the behaviors of endothelial cells, Schwann cells, and fibroblasts cultured with serum from differently treated macrophages (Fig. 6A1 and Fig. S9, Supporting Information). In the AFG<sup>KLT</sup>-treated group, genetic expression of VEGF and PDGF in HUVECs, as well as MBP and BDNF in RSC-96 cells, was significantly upregulated. In contrast, the TCP group (macrophages treated with LPS & IFN- $\gamma$  only) exhibited the lowest levels of expression (Fig. 6A2 and A4). Additionally, cellular spreading and cytoskeletal extension of HUVECs and RSC-96 cells were more pronounced in the AFG<sup>KLT</sup> group compared to the contracted cellular configuration in the TCP group, indicating better cellular viability in the less intense pro-inflammatory microenvironment alleviated by AFG<sup>KLT</sup> modulation (Fig. 6A3 and A5). A similar trend was observed in the fibroblast recruitment assessment, with a significantly increased number of cells recruited in the AFG<sup>KLT</sup> group, whereas minimal cell migration occurred in the TCP groups (Fig. 6A6 and A7). These findings suggested that the AFG<sup>KLT</sup> hydrogel may facilitate the anti-inflammatory transition, thereby enhancing pro-regenerative crosstalk between macrophages and endothelial cells, Schwann cells, and fibroblasts. The modulated interactions facilitated by the dual signals delivered by AFG<sup>KLT</sup>

hydrogels promoted cell viability and behaviors such as vascularization, myelination, and migration, demonstrating successful optimization of the immune microenvironment.

Subsequently, we investigated the angiogenic microenvironment by indirectly co-culturing Schwann cells or fibroblasts with differently treated endothelial cells (Fig. 6B1 and Fig. S10, Supporting Information). The results demonstrated that the AFG<sup>KLT</sup>-treated HUVECs upregulated the genetic expression of MBP and BDNF in Schwann cells, which are key markers of myelination and neural support, respectively (Fig. 6B2). Additionally, these Schwann cells exhibited accelerated cytoskeletal elongation, indicating enhanced cellular morphogenesis and functional maturation (Fig. 6B3). In the case of fibroblasts, those cultured in the serum from AFG<sup>KLT</sup>-treated HUVECs showed significantly enhanced proliferation, as revealed in the CCK-8 assessment and bright field observation (Fig. 6B4 and B5). This indicated that the factors secreted by the AFG<sup>KLT</sup>-treated HUVECs create a conducive environment for fibroblast growth. The observed effects are possibly attributed to the enhanced secretion of various cytokines and growth factors from the endothelial cells treated with AFG<sup>KLT</sup> hydrogels. The optimized angiogenic microenvironment, induced by the AFG<sup>KLT</sup> hydrogels, promotes the maturation of Schwann cells and the proliferation of fibroblasts, enhancing intercellular communication, which is crucial for tissue repair and regeneration, particularly in diabetic wound healing.

Furthermore, HUVECs and L929 cells were indirectly co-cultured with RSC-96 cells to investigate crosstalk facilitation in the neural microenvironment (Fig. 6C1 and Fig. S11, Supporting Information). Notably, HUVECs co-cultured in the AFG<sup>KLT</sup> group exhibited significantly upregulated expression of VEGF and PDGF, along with observable vascularizing morphogenesis (Fig. 6C2 and C3). This suggested that the angiogenic behaviors of endothelial cells were prominently facilitated by the enhanced secretion from Schwann cells treated with AFG<sup>KLT</sup>, highlighting the importance of neuro-vascular development. Additionally, the gene and protein expression levels of  $\alpha$ -SMA in fibroblasts were significantly higher in the AFG<sup>KLT</sup> group compared to other groups (Fig. 6C4 and C5). This indicated positive activation of fibroblasts towards a myofibroblast phenotype, which plays a crucial role in remodeling the ECM orientation. The AFG<sup>KLT</sup> hydrogel significantly strengthened the secretion capacity of Schwann cells, including the secretion of VEGF and TGF- $\beta$ , underscoring the positive facilitation of crosstalk between Schwann cell maturation and endothelial cell

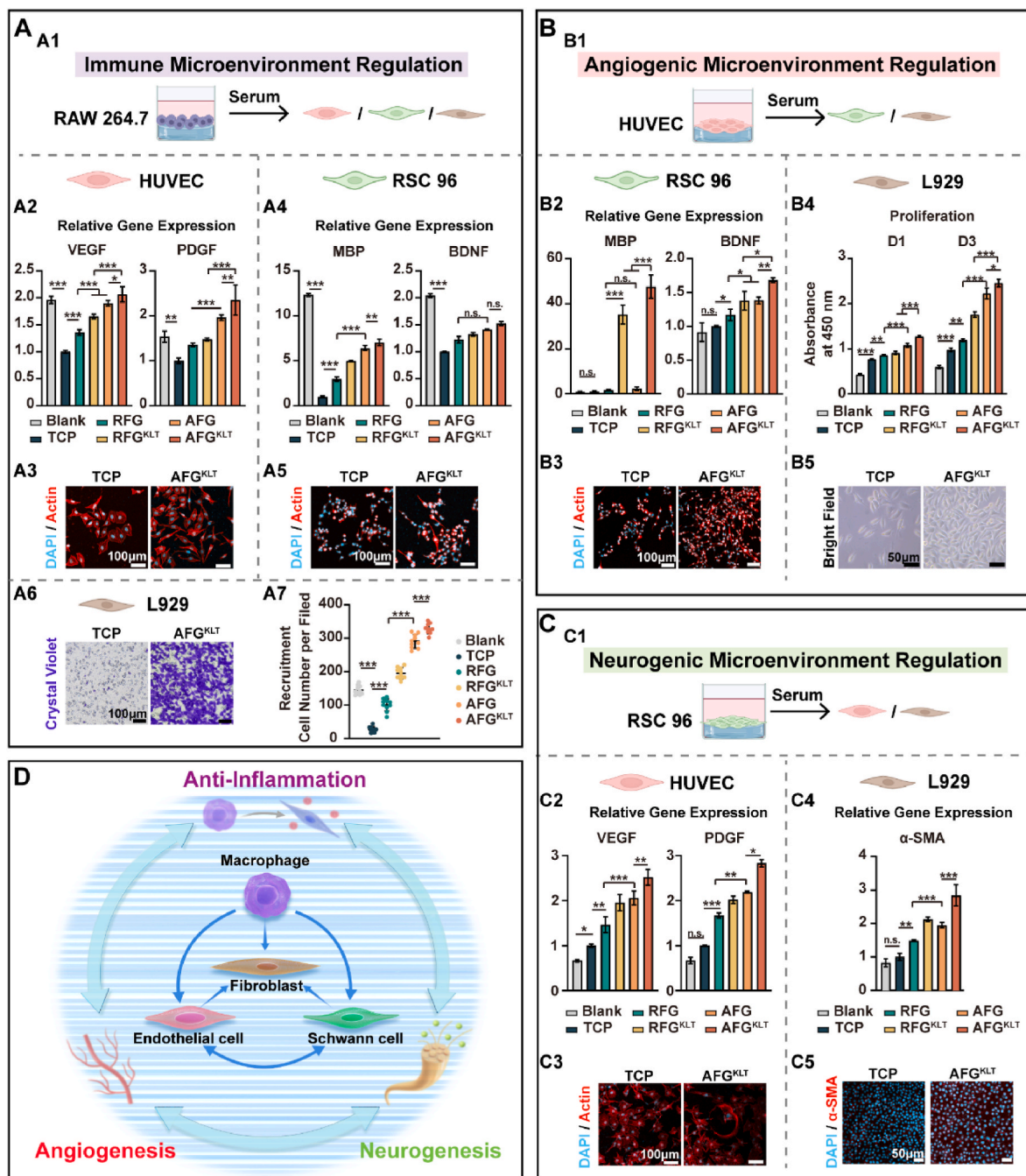


**Fig. 6.** AFG<sup>KLT</sup> hydrogels modulated inter-microenvironmental crosstalk. A) Schematic diagram of HUVEC, RSC-96, and L929 cultured in the serum of RAW 264.7 cultivated on different hydrogels (A1). Relative gene expression (A2, A4) and cytoskeleton staining images (A3, A5) of HUVEC or RSC-96 at 72 h, quantitative analysis (A6) and representative photographs (A7) from recruitment assay of L929 at 24 h indirectly co-cultured with RAW 264.7. B) Schematic diagram of RSC-96 and L929 cultured in the serum of HUVEC cultivated on different hydrogels (B1). Relative gene expression (B2) and cytoskeleton staining images (B3) of RSC-96, quantitative analysis in proliferation CCK-8 assay (B4), and representative bright field photographs (B5) of L929 indirectly co-cultured with HUVEC for 72 h. C) Schematic diagram of HUVEC and L929 cultured in the serum of RSC-96 cultivated on different hydrogels (C1). Relative gene expression (C2) and cytoskeleton staining images (C3) of HUVEC, relative gene expression (C4), and α-SMA immunostaining images (C5) of L929 indirectly co-cultured with HUVEC for 72 h. D) General illustration of triadic interactions among immune-angiogenic-neurogenic microenvironment.

vascularization or fibroblast activation. These findings further evidence the optimization of the neural microenvironment by AFG<sup>KLT</sup> hydrogels.

Overall, our findings demonstrated that AFG<sup>KLT</sup> hydrogel significantly enhanced multicellular crosstalk by optimizing the microenvironment through specific cell modulation using dual signals: oriented fibrous guidance and bioactive peptide enhancement. These results indicated that AFG<sup>KLT</sup> hydrogels effectively refine the multidimensional microenvironment *in vitro*, with the triadic synergy of immune-

angiogenic-neurogenic microenvironments highlighting their potential as dressings for promoting diabetic wound healing.

**3.7. AFG<sup>KLT</sup> hydrogel accelerated diabetic wound healing and matrix reconstruction *in vivo***

To comprehensively assess the regenerative effects of the bioactive anisotropic nanofiber hydrogel in diabetic wound healing, we

conducted an *in vivo* test using a full-thickness skin defect model in STZ-induced diabetic rats. We created a 2-cm diameter incision on the dorsum of each rat, then treated the wounds with AFG<sup>KLT</sup>, AFG, RFG<sup>KLT</sup>, or RFG hydrogels as wound dressings. The control group received saline treatment. The wound-healing process was evaluated through weekly observations and histological analysis to elucidate the promising impacts of the bioactive aligned hydrogel (Fig. 7A).

As shown in Fig. 7B, the AFG<sup>KLT</sup> group exhibited the smallest wound area at all time points compared to the other groups, while the control group showed minimal regeneration. The unsatisfactory wound healing outcomes in the control group indicated the successful establishment of a chronic diabetic wound model, characterized by poor self-healing capacity without any treatment. In contrast, the defects in the AFG<sup>KLT</sup> group were nearly completely healed, demonstrating the significant potential of AFG<sup>KLT</sup> in accelerating diabetic wound healing, as evidenced by the most rapid wound closure trend displayed in the representative heat map (Fig. 7C). It is worth noting that, the shape of wounds in the AFG and AFG<sup>KLT</sup> groups showed gradual deformation from circular incisions towards elongated elliptical configuration, ultimately forming a slit-like shape. These results suggested that the aligned fibrous structures might significantly guide and accelerate wound closure by promoting cellular directional extension and oriented alignment, as elucidated *in vitro*. The quantified wound area also highlighted the promising regenerative effect of AFG<sup>KLT</sup> hydrogel in promoting diabetic wound healing, with consistently the smallest wound area among all groups at all time points (Fig. 7D). On Day 7, the wound area of the AFG<sup>KLT</sup> group was  $73.30 \pm 3.39\%$ , significantly smaller than the control group ( $86.62 \pm 3.25\%$ ), indicating that the dual modulation of physical and bioactive cues in the AFG<sup>KLT</sup> can expedite the wound healing from the early stages. Additionally, the statistics demonstrated that the hydrogels with aligned fibrous structures (AFG and AFG<sup>KLT</sup>) or bioactive functionalization (RFG<sup>KLT</sup> and AFG<sup>KLT</sup>) were more effective in reducing the diabetic wound area compared to the random fibrous hydrogel (RFG and RFG<sup>KLT</sup>) and unfunctionalized hydrogel (RFG and AFG), respectively. This finding highlighted the outstanding role of dual physical and bioactive cues in promoting skin defect closure.

Furthermore, histological analysis was conducted to assess tissue regeneration and wound development. Representative H&E staining images depicted the tissue regeneration process in diabetic wound healing on Day 7 and Day 28, revealing that tissue regeneration was most prominent in the AFG<sup>KLT</sup> group, consistent with the wound closure outcomes (Fig. 7E). The AFG<sup>KLT</sup> group demonstrated the most promising regenerative effects, exhibiting the greatest epithelial thickness and the smallest wound width at the defect site on Day 28 post-surgery (Fig. 7F and G). These findings suggested that the AFG<sup>KLT</sup> hydrogel effectively reconstructs subcutaneous tissue and reinforces incisional closure, thereby enhancing the full-thickness wound healing process.

The deposition of collagen and keratin filaments can effectively facilitate the maturation of the regenerated epidermis layer during wound healing [84]. To further evaluate the maturation of regenerated skin tissue, Masson staining and K14 immunostaining were conducted on Day 28 post-surgery (Fig. 7H and I). The most effective collagen accumulation was shown in the AFG<sup>KLT</sup> group, with the highest collagen deposition ratio of  $70.07 \pm 4.68\%$  in the Masson staining images (Fig. 7J). Additionally, the AFG<sup>KLT</sup> group exhibited prominent K14-positive keratin filaments with follicle-like configuration and a significantly increased number of dermal appendages (Fig. 7K). These results manifested that the AFG<sup>KLT</sup> hydrogel might greatly promote the maturation of regenerated skin tissue, characterized by organized collagen deposition and effective follicle formation, which are crucial for the functional recovery of repaired skin.

Our findings highlighted that the bioactive anisotropic hydrogel can efficiently accelerate diabetic wound healing, owing to the synergistic effects of dual cues: physically oriented guidance and bioactive modulation. As shown in the magnified regions of H&E and Masson staining, the organized alignment of tissue fibers and cellular matrix were

observed in the treatment group with aligned fibrin hydrogels, whereas more compact overlays were evident in the regenerated tissue in the bioactive hydrogel groups, respectively (Fig. S12, Supporting Information).

### 3.8. AFG<sup>KLT</sup> hydrogel modulated the triadic synergy of immune-angiogenic-neurogenic microenvironments *in vivo*

To elucidate the underlying mechanisms behind the promising regenerative effects of AFG<sup>KLT</sup> on diabetic wound healing, various immunostaining was conducted for detailed histological analysis. Encouraged by the satisfactory multicellular modulation capabilities of AFG<sup>KLT</sup> *in vitro*, we propose that the dual function of oriented anisotropic structures and pro-angiogenic peptides may refine the multidimensional microenvironment in diabetic wounds, thereby enhancing skin tissue regeneration and accelerating wound healing.

The immune dysregulation in diabetic wounds is characterized by imbalanced and chronic pro-inflammatory responses, inhibiting tissue regeneration. The immune microenvironment in the early stage was evaluated using CD86 (pro-inflammatory marker) and CD206 (anti-inflammatory marker) immunostaining on Day 7 and Day 14. As shown in Fig. 8A, the control group exhibited intense CD86-positive expression and minimal CD206 expression on both Day 7 and Day 14, indicating dysregulated acute inflammatory responses and the formation of chronic immune pathology in diabetic wounds. In contrast, the AFG and AFG<sup>KLT</sup> groups demonstrated comparably greater CD206 expression on Day 7 and significantly reduced CD86 expression on Day 14. The quantified CD86-positive (Fig. 8E) and CD206-positive (Fig. 8F) cell ratio showed significantly less pro-inflammatory and increased anti-inflammatory macrophages in the AFG and AFG<sup>KLT</sup> groups compared to the RFG and RFG<sup>KLT</sup> groups, respectively, on both Day 7 and Day 14. Additionally, the refinement of the immune microenvironment was further assessed using two key inflammatory cytokine markers, TNF- $\alpha$  and IL-10. Compared to other groups, wounds treated with AFG<sup>KLT</sup> displayed significantly enhanced expression of IL-10, a pro-regenerative cytokine associated with anti-inflammatory macrophages, while markedly suppressing the expression of TNF- $\alpha$ , a pro-inflammatory cytokine (Fig. S13, Supporting Information). Statistical analysis of the positive staining area revealed that the AFG<sup>KLT</sup> group exhibited the highest IL-10 expression and the lowest TNF- $\alpha$  expression, underscoring its efficacy in promoting an anti-inflammatory microenvironment. Collectively, these results suggested that aligned structural guidance can significantly enhance anti-inflammatory modulation, optimize the immune microenvironment with balanced inflammation, and prevent chronic wound formation. Structural alignment appears to regulate macrophage polarization through shape-induced mechanisms, as evidenced *in vitro*, facilitating the proper transition of macrophages from inflammation to proliferation during wound healing. This modulation is crucial for developing a pro-regenerative microenvironment *in vivo*.

Furthermore, we focused on angiogenesis and neurogenesis outcomes during the proliferation phase on Day 28. Immunostaining for CD31 and S100 depicted neovascularization and skin nerve regeneration in diabetic wounds, respectively (Fig. 8B). Notably, tube-like vascular configurations with CD31-positive expression were significantly observable in the RFG<sup>KLT</sup> and AFG<sup>KLT</sup> groups, while these configurations were less apparent in other groups, revealing that the angiogenesis was significantly enhanced with the incorporation of bioactive motifs. The aligned topographical guidance might also amplify the vascularization by guiding the vascular extension and elongation in the wound sites, as evidenced by the highest CD31-positive expression area in the AFG<sup>KLT</sup> group (Fig. 8G). Additionally, the regenerated skin nerve maturation could be visualized with the myelination protein, S100, presenting the staple-like fiber conformation in the AFG and AFG<sup>KLT</sup> groups. Along with the quantified result of significantly elevated S100-positive area percentage in the AFG<sup>KLT</sup> group (Fig. 8H), it is evident that the aligned fibrous structure plays crucial roles in facilitating neurogenesis at the

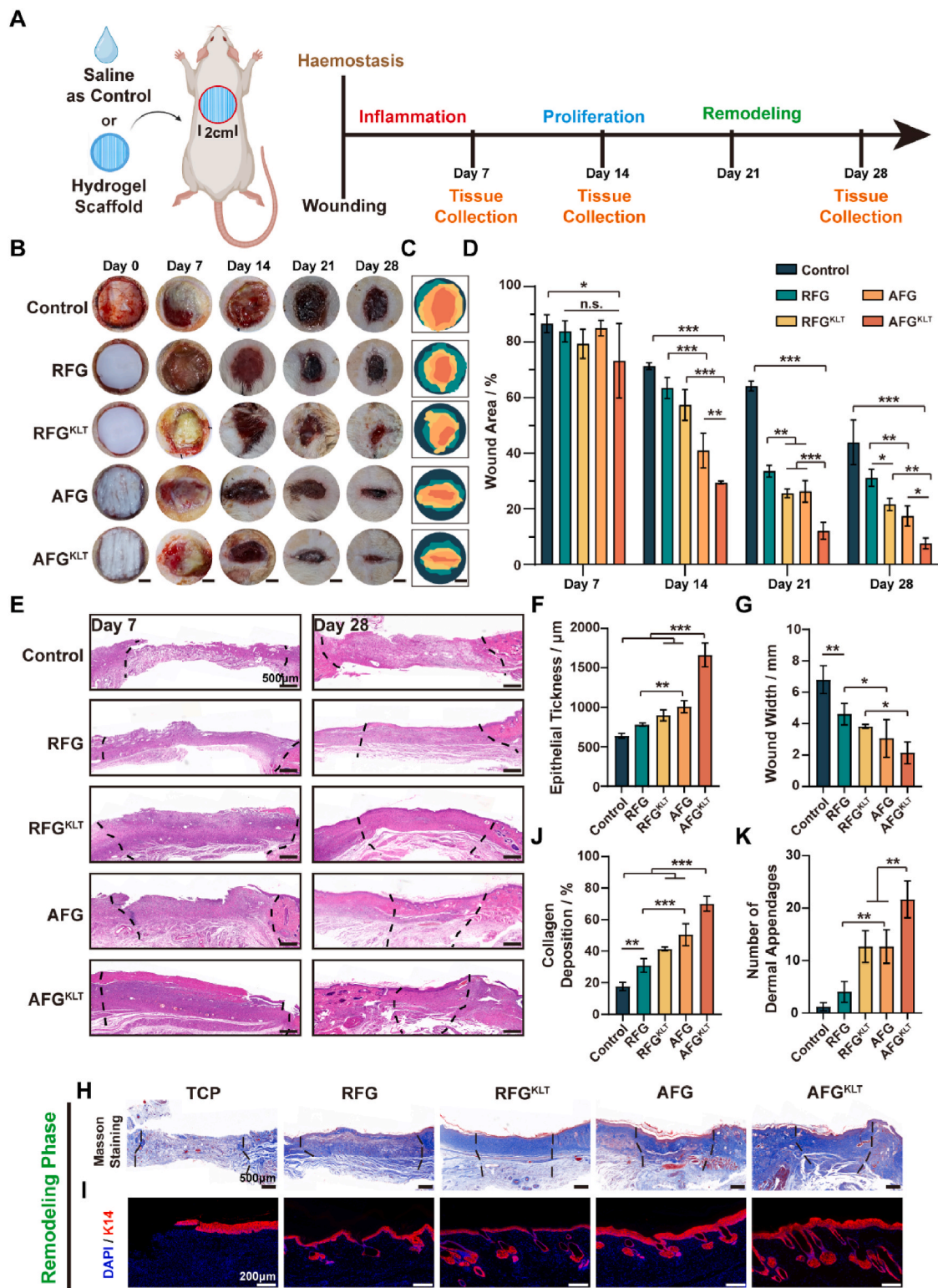
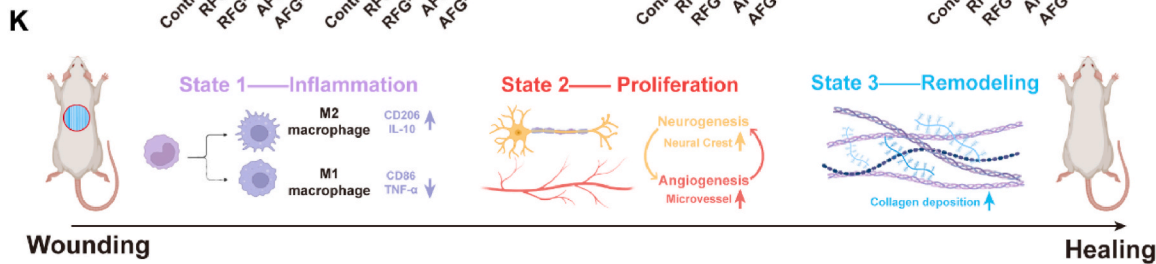
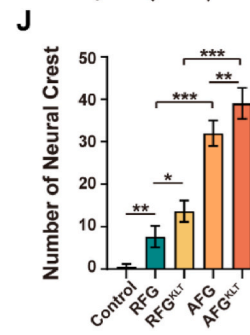
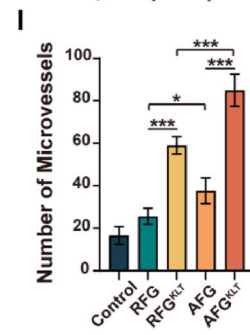
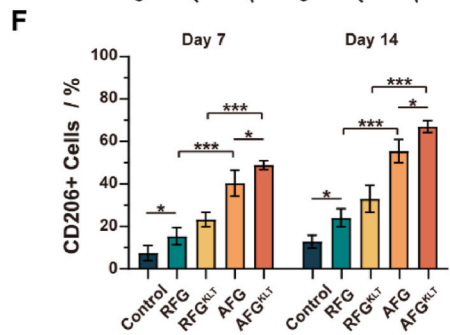
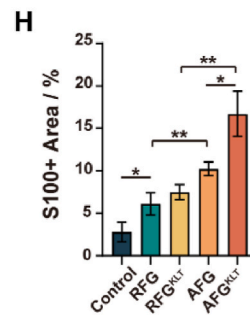
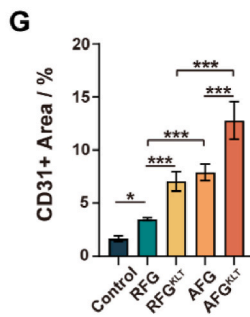
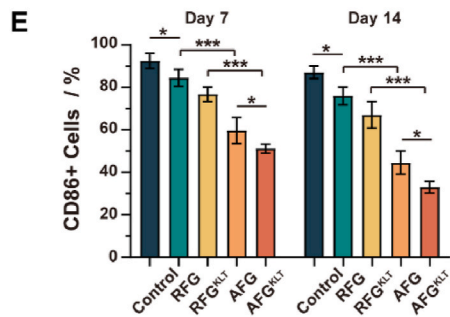
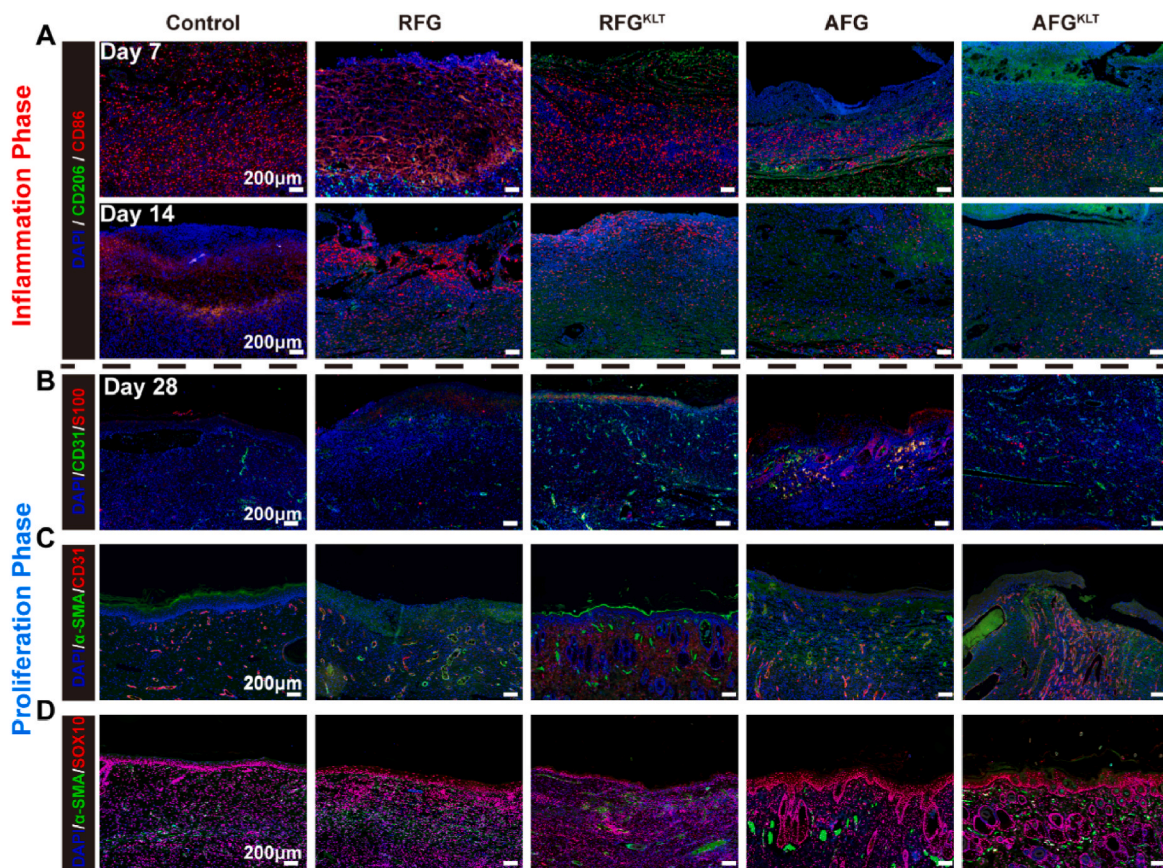


**Fig. 7.** AFG<sup>KLT</sup> hydrogel accelerated diabetic wound healing and matrix reconstruction. A) Schematic diagram of animal experiments and tissue collection timeline. B) Representative photographs of the diabetic wounds in different treatment groups on Day 0, Day 7, Day 14, Day 21, and Day 28 post-surgery. C) Schematic diagram of wound healing process in different treatment groups. D) Quantification analysis of wound area in different treatment groups on Day 7, Day 14, Day 21, and Day 28 post-surgery. E) Representative H&E staining images of different treatment groups on Day 7 and Day 28 post-surgery; the dotted lines indicate the boundary of the lesion sites. F, G) Quantification analysis of the epithelial thickness (F) and wound width (G) of different treatment groups on Day 28 post-surgery from the H&E staining images. H) Representative images of Masson staining of different treatment groups on Day 28 post-surgery; the dotted lines indicate the boundary of the lesion sites. I) Representative immunofluorescence staining with K14 (red) and DAPI (blue) of different treatment groups on Day 28 post-surgery. J) Quantification analysis of collagen deposition percentage from the Masson staining J) Quantification analysis of the average number of dermal appendages from the immunostaining of K14. The bar plot data is represented in mean  $\pm$  standard deviation. \*P < 0.05, \*\*P < 0.01, \*\*\*P < 0.001, n.s. no significant.



(caption on next page)



**Fig. 8.** AFG<sup>KLT</sup> hydrogel modulated the triadic synergy of Immune-Angiogenic-Neurogenic microenvironments. A) Representative immunostaining images of tissue sections in different treatment groups at Day 7 and Day 14 post-surgery with CD86 (red), CD206 (green), and DAPI (blue). B–D) Representative immunostaining images of tissue sections in the different treatment groups at Day 28 post-surgery with (B) S100 (red), CD31 (green) and DAPI (blue); (C) CD31 (red),  $\alpha$ -SMA (green) and DAPI (blue); (D) SOX10 (red),  $\alpha$ -SMA (green) and DAPI (blue). E, F) Quantification analysis of CD86-positive cells (E) and CD206-positive cells (F) from CD86<sup>+</sup>CD206 co-staining images. G, H) Quantification analysis of CD31-positive (G) and S100-positive (H) area percentage from CD31-S100 co-staining images. I) Quantification analysis of the number of microvessels from CD31- $\alpha$ -SMA co-staining images. J) Quantification analysis of the number of neural crests from SOX10- $\alpha$ -SMA co-staining images. K) Schematic illustration of wound healing map and potential mechanism.

wound site, while the bioactive peptides might exhibit a synergistic effect via reinforcing cellular adhesion and myelination. The ideal angiogenic and neurogenic properties of the AFG<sup>KLT</sup> might be underscored by modulating endothelial cell vascularization and Schwann cell maturation, as confirmed *in vitro* with consistent findings. Moreover, the co-staining of CD31 and S100 demonstrated the favorable reconstruction of the neurovascular niche in the AFG<sup>KLT</sup> group, with cross-connections of regenerated vessels and nerves observed.

Subsequently, the refinement of vascular and neural microenvironments was investigated with co-staining of CD31 or SOX10 with  $\alpha$ -SMA ( $\alpha$ -smooth muscle actin) (Fig. 8C and D). The tubular structures formed with positive CD31 and  $\alpha$ -SMA represent the microvessels in the wound sites [85–87]. The AFG<sup>KLT</sup> group exhibited the most prominent angiogenesis, with  $85.0 \pm 7.5$  newly established microvessels (Fig. 8I), suggesting that the AFG<sup>KLT</sup> hydrogel might resolve the impaired angiogenesis in diabetic wounds, optimizing the vascular microenvironment with improved vessel support and substance transportation for diabetic wound healing. Although the RFG<sup>KLT</sup> group demonstrated high CD31 expression, the lack of dual positivity with  $\alpha$ -SMA and tubular structures suggests an early stage of vascularization without the formation of mature and functional microvessels. This highlights the critical role of the anisotropic structure and KLT peptide bioactivity in promoting both the initiation and maturation of neovascularization in the AFG<sup>KLT</sup> group. In the meanwhile, SOX10, a nucleocytoplasmic shuttling protein highly expressed in the newly born nerves and neural crests in the skin tissues, was abundantly co-expressed with  $\alpha$ -SMA in the AFG<sup>KLT</sup> group, forming circular conformations [88]. The quantified result demonstrated a significantly increased number of neural crests ( $39.0 \pm 3.6$ ) formed in the wound sites (Fig. 8J). These results indicated that the AFG<sup>KLT</sup> hydrogel significantly facilitates the neural microenvironment, accelerating skin nerve regeneration and maturation.

Collectively, the histological analysis highlights that the incorporation of aligned fibrous structures and pro-angiogenic bioactive peptides in the AFG<sup>KLT</sup> hydrogel refined the triadic synergy of immune-angiogenic-neurogenic microenvironments in diabetic wounds, thereby promoting skin tissue regeneration and wound healing.

Anisotropic structural biomaterials for tissue engineering have been extensively applied in the regeneration therapy of directionally oriented tissues such as nerves, ligaments, and muscles. However, its potential in non-directed tissue repair has been relatively underexplored. Given the fact that natural tissues are inherently oriented with cells and matrix assembling across multiple scales, the significance of anisotropic structure is highlighted by the capability of regulating various cellular behaviors for remodeling the tissue matrix. As an example, our previous studies have demonstrated that, in brain tissue, anisotropic hydrogel can facilitate the migration of neural stem cells and promote neurogenesis [89]. Nevertheless, the integration of oriented structures in biomaterials for skin wound repair has not yet been explored widely. Skin regeneration and scar formation are closely linked to mechanical forces and tissue tension, as tension reduction of the wounded skin has been considered vital in minimizing scar formation. Modulation over bio-mechanics, including cellular mechanosensing and mechanotransduction, with anisotropic structures proposes great potential and a new strategy for skin tissue regeneration. Our research has further confirmed that anisotropy, through the modulation of multiple cellular processes, can establish an immune-vascular-neural regenerative microenvironment, thereby enhancing skin tissue regeneration. In diabetic wounds, where healing is impeded by complex

microenvironmental factors, our approach of integrating oriented structures has enabled the efficient and synergistic regulation of multiple microenvironments, demonstrating promising translational potential. In particular, by incorporating VEGF-mimicking short peptides, we significantly enhanced vascularization, the pivotal phase in diabetic wound healing—thereby further boosting the therapeutic effects of the oriented structures of the hydrogel. Interestingly, we observed that along the direction of fiber orientation, the wounded skin tissue exhibited faster regenerative speed. This inspired us to think that when the aligned direction of anisotropic hydrogels was directionally parallel to the wound's shortest axis, the promotion of wound healing might be maximized. In our future work, we would like to develop an anisotropic wound model (square and rectangular) to figure out this interesting finding.

#### 4. Conclusion

In summary, we successfully fabricated a bioactive anisotropic nanofiber hydrogel through fibrin electrospinning and self-assembling peptide modification. This hydrogel exhibited the dual impacts of ideal nano-scaled fibrous alignment and prominent pro-angiogenic bioactivity for promoting diabetic wound healing by harnessing the triadic synergy of the immune-angiogenic-neurogenic microenvironment. Our results elucidated that highly oriented nanofibers significantly modulated multicellular behaviors, including the facilitation of endothelial cell vascularization, shape-induced anti-inflammatory transitions in macrophages, morphogenetic maturation of Schwann cells, and oriented ECM deposition by fibroblasts, showcasing the capacity for optimization of multiple microenvironments. Notably, the enhanced angiogenic features strengthened the inter-phase crosstalk, maximizing the interlocking connections of the immune-angiogenic-neurogenic niche. Further, the bioactive anisotropic nanofiber hydrogel significantly accelerated wound healing and efficient matrix reconstruction in the diabetic rat model. Taken together, our work highlighted the significance of modulating the multidimensional microenvironment with a simple anisotropic structure, advancing its effectiveness in chronic wound healing.

#### CRedit authorship contribution statement

**Kunkoo Kim:** Writing – review & editing, Writing – original draft, Validation, Methodology, Investigation, Funding acquisition, Formal analysis, Conceptualization. **Jia Yang:** Writing – review & editing, Writing – original draft, Methodology, Investigation, Formal analysis. **Chengli Li:** Validation, Resources, Methodology, Investigation. **Chun-Yi Yang:** Resources, Methodology, Investigation, Supervision, Writing – review & editing. **Peilun Hu:** Validation, Methodology, Investigation. **Yaosai Liu:** Validation, Methodology, Formal analysis. **Yin-yuan Huang:** Validation, Formal analysis. **Xiaohan Sun:** Methodology, Investigation. **Ming Chi:** Methodology, Investigation. **Chenyu Huang:** Methodology, Validation. **Xiaodan Sun:** Validation, Formal analysis. **Lingyun Zhao:** Formal analysis, Investigation. **Xiumei Wang:** Writing – review & editing, Validation, Supervision, Resources, Project administration, Methodology, Investigation, Funding acquisition, Conceptualization.

## Ethics approval and consent to participate

Animal experiments of this study were performed in strict accordance with the Guide for Care and Use of Laboratory Animals of the National Institutes of Health, and all animal procedures were evaluated and granted by the Institutional Animal Care and Use Committee of Tsinghua University (Beijing, China, approval number: 22-WXM3).

## Declaration of competing interest

The authors declare that they have no known competing financial interests or personal relationships that could have appeared to influence the work reported in this paper.

## Acknowledgments

The authors thank the financial support from the Beijing Natural Science Foundation of China (Grant No. QY23102, 2254091, and L234075) and the National Natural Science Foundation of China (Grant No. 32271414, 32401140, and 82301560). Schematic icons in Figs. 6 and 8 are created with BioRender.com.

## Appendix A. Supplementary data

Supplementary data to this article can be found online at <https://doi.org/10.1016/j.bioactmat.2025.01.004>.

## References

- [1] S.B. Bashar, Shape the Future of Diabetes at the IDF World Diabetes Congress 2022, ELSEVIER IRELAND LTD ELSEVIER HOUSE, BROOKVALE PLAZA, EAST PARK SHANNON, CO, 2022.
- [2] V. Falanga, Wound healing and its impairment in the diabetic foot, *Lancet* 366 (9498) (2005) 1736–1743.
- [3] J.L. Burgess, W.A. Wyant, B. Abdo Abujamra, R.S. Kirsner, I. Jozic, Diabetic wound-healing science, *Medicina* 57 (10) (2021) 1072.
- [4] A.L. Dellon, Nerve decompression in diabetics with chronic nerve compression: update 2022, *Plastic and Aesthetic Research* 9 (7) (2022) 45.
- [5] J. Shan, J. Che, C. Song, Y. Zhao, Emerging antibacterial nanozymes for wound healing, *Smart Medicine* 2 (3) (2023) e20220025.
- [6] G.C. Gurtner, S. Werner, Y. Barrandon, M.T. Longaker, Wound repair and regeneration, *Nature* 453 (7193) (2008) 314–321.
- [7] P. Cheng, X. Xie, L. Hu, W. Zhou, B. Mi, Y. Xiong, H. Xue, K. Zhang, Y. Zhang, Y. Hu, Hypoxia endothelial cells-derived exosomes facilitate diabetic wound healing through improving endothelial cell function and promoting M2 macrophages polarization, *Bioact. Mater.* 33 (2024) 157–173.
- [8] Y. Xiong, Z. Lin, P. Bu, T. Yu, Y. Endo, W. Zhou, Y. Sun, F. Cao, G. Dai, Y. Hu, A whole-course-repair system based on neurogenesis-angiogenesis crosstalk and macrophage reprogramming promotes diabetic wound healing, *Adv. Mater.* 35 (19) (2023) 2212300.
- [9] S. He, Z. Li, L. Wang, N. Yao, H. Wen, H. Yuan, J. Zhang, Z. Li, C. Shen, A nanoenzyme-modified hydrogel targets macrophage reprogramming-angiogenesis crosstalk to boost diabetic wound repair, *Bioact. Mater.* 35 (2024) 17–30.
- [10] S. Shang, K. Zhuang, J. Chen, M. Zhang, S. Jiang, W. Li, A bioactive composite hydrogel dressing that promotes healing of both acute and chronic diabetic skin wounds, *Bioact. Mater.* 34 (2024) 298–310.
- [11] F. Shu, H. Huang, S. Xiao, Z. Xia, Y. Zheng, Netrin-1 co-cross-linked hydrogel accelerates diabetic wound healing in situ by modulating macrophage heterogeneity and promoting angiogenesis, *Bioact. Mater.* 39 (2024) 302–316.
- [12] J. Yang, K. Yang, W. Man, J. Zheng, Z. Cao, C.Y. Yang, K. Kim, S. Yang, Z. Hou, G. Wang, X. Wang, 3D bio-printed living nerve-like fibers refine the ecological niche for long-distance spinal cord injury regeneration, *Bioact. Mater.* 25 (2023) 160–175.
- [13] Q. Hou, K. Liu, C. Lian, J. Liu, W. Wei, T. Qiu, H. Dai, A gelatin-based composite hydrogel with a “one stone, two birds” strategy for photothermal antibacterial and vascularization of infected wounds, *Biomacromolecules* 24 (7) (2023) 3397–3410.
- [14] M.J. Dalby, N. Gadegaard, R.O. Oreffo, Harnessing nanotopography and integrin-matrix interactions to influence stem cell fate, *Nat. Mater.* 13 (6) (2014) 558–569.
- [15] J.H. Wen, L.G. Vincent, A. Fuhrmann, Y.S. Choi, K.C. Hribar, H. Taylor-Weiner, S. Chen, A.J. Engler, Interplay of matrix stiffness and protein tethering in stem cell differentiation, *Nat. Mater.* 13 (10) (2014) 979–987.
- [16] B. Yi, Q. Xu, W. Liu, An overview of substrate stiffness guided cellular response and its applications in tissue regeneration, *Bioact. Mater.* 15 (2022) 82–102.
- [17] H. Kang, Z. Xu, Y. Huang, K. Liu, W. Wei, L. Xu, S. Gao, D. Hong, X. Wu, Y. Zhao, H. Dai, Molecular design boosts hydrolytic stability of diisopropanolamine boronic ester hydrogel for long-term drug release, *Chem. Mater.* 36 (15) (2024) 7232–7242.
- [18] X. Fu, J. Wang, D. Qian, Z. Chen, L. Chen, W. Cui, Y. Wang, Living electrospun short fibrous sponge via engineered nanofat for wound healing, *Advanced Fiber Materials* 5 (3) (2023) 979–993.
- [19] X. Fu, J. Wang, D. Qian, L. Xi, L. Chen, Y. Du, W. Cui, Y. Wang, Oxygen atom-concentrating short fibrous sponge regulates cellular respiration for wound healing, *Advanced Fiber Materials* 5 (5) (2023) 1773–1787.
- [20] C.-Y. Yang, Z. Hou, P. Hu, C. Li, Z. Li, Z. Cheng, S. Yang, P. Ma, Z. Meng, H. Wu, Y. Pan, Z. Cao, X. Wang, Multi-needle blow-spinning technique for fabricating collagen nanofibrous nerve guidance conduit with scalable productivity and high performance, *Materials Today Bio* 24 (2024) 100942.
- [21] B. Jin, Y. Yu, C. Lou, X. Zhang, B. Gong, J. Chen, X. Chen, Z. Zhou, L. Zhang, J. Xiao, J. Xue, Combining a density gradient of biomacromolecular nanoparticles with biological effectors in an electrospun fiber-based nerve guidance conduit to promote peripheral nerve repair, *Adv. Sci.* 10 (4) (2023) 2203296.
- [22] S. Yao, Y. Yang, C. Li, K. Yang, X. Song, C. Li, Z. Cao, H. Zhao, X. Yu, X. Wang, L.-N. Wang, Axon-like aligned conductive CNT/GelMA hydrogel fibers combined with electrical stimulation for spinal cord injury recovery, *Bioact. Mater.* 35 (2024) 534–548.
- [23] R. Hao, X. Ye, X. Chen, J. Du, F. Tian, L. Zhang, G. Ma, F. Rao, J. Xue, Integrating bioactive graded hydrogel with radially aligned nanofibers to dynamically manipulate wound healing process, *ACS Appl. Mater. Interfaces* 16 (29) (2024) 37770–37782.
- [24] A. Saraswathibhatla, D. Indana, O. Chaudhuri, Cell-extracellular matrix mechanotransduction in 3D, *Nat. Rev. Mol. Cell Biol.* 24 (7) (2023) 495–516.
- [25] S. Zhang, X. Liu, S.F. Barreto-Ortiz, Y. Yu, B.P. Ginn, N.A. DeSantis, D.L. Hutton, W. L. Grayson, F.Z. Cui, B.A. Korgel, S. Gerecht, H.Q. Mao, Creating polymer hydrogel microfibrils with internal alignment via electrical and mechanical stretching, *Biomaterials* 35 (10) (2014) 3243–3251.
- [26] M.H. Norahan, S.C. Pedroza-González, M.G. Sánchez-Salazar, M.M. Álvarez, G. Trujillo de Santiago, Structural and biological engineering of 3D hydrogels for wound healing, *Bioact. Mater.* 24 (2023) 197–235.
- [27] Y. Sun, Y. Zhang, Y. Guo, D. He, W. Xu, W. Fang, C. Zhang, Y. Zuo, Z. Zhang, Electrical aligned polyurethane nerve guidance conduit modulates macrophage polarization and facilitates immunoregulatory peripheral nerve regeneration, *J. Nanobiotechnol.* 22 (1) (2024) 244.
- [28] G. Tseropoulos, P. Mehrotra, A.K. Podder, E. Wilson, Y. Zhang, J. Wang, A. Koontz, N.P. Gao, R. Gunawan, S. Liu, L.M. Feltri, M.E. Bronner, S.T. Andreadis, Immunoblast NRG1 accelerates neural crest like cell differentiation toward functional schwann cells through sustained erk1/2 activation and YAP/TAZ nuclear translocation, *Adv. Sci.* (2024) e2402607.
- [29] X. Wang, K. Sun, C. Wang, M. Yang, K. Qian, B. Ye, X. Guo, Y. Shao, C. Chu, F. Xue, J. Li, J. Bai, Ultrasound-responsive microfibers promoted infected wound healing with neuro-vascularization by segmented sonodynamic therapy and electrical stimulation, *Biomaterials* 313 (2025) 122803.
- [30] G. Chen, X. Gao, J. Chen, L. Peng, S. Chen, C. Tang, Y. Dai, Q. Wei, D. Luo, Actomyosin activity and Piezo1 activity synergistically drive urinary system fibroblast activation, *Adv. Sci.* 10 (33) (2023) e2303369.
- [31] C.-Y. Yang, Z. Meng, K. Yang, Z. He, Z. Hou, J. Yang, J. Lu, Z. Cao, S. Yang, Y. Chai, External magnetic field non-invasively stimulates spinal cord regeneration in rat via a magnetic-responsive aligned fibrin hydrogel, *Biofabrication* 15 (3) (2023) 035022.
- [32] S. Yao, F. He, Z. Cao, Z. Sun, Y. Chen, H. Zhao, X. Yu, X. Wang, Y. Yang, F. Rosei, Mesenchymal stem cell-laden hydrogel microfibers for promoting nerve fiber regeneration in long-distance spinal cord transection injury, *ACS Biomater. Sci. Eng.* 6 (2) (2020) 1165–1175.
- [33] J. Du, J. Liu, S. Yao, H. Mao, J. Peng, X. Sun, Z. Cao, Y. Yang, B. Xiao, Y. Wang, Prompt peripheral nerve regeneration induced by a hierarchically aligned fibrin nanofiber hydrogel, *Acta Biomater.* 55 (2017) 296–309.
- [34] S. Yang, J. Zhu, C. Lu, Y. Chai, Z. Cao, J. Lu, Z. Zhang, H. Zhao, Y.-Y. Huang, S. Yao, Aligned fibrin/functionalized self-assembling peptide interpenetrating nanofiber hydrogel presenting multi-cues promotes peripheral nerve functional recovery, *Bioact. Mater.* 8 (2022) 529–544.
- [35] C.-Y. Yang, Z. Meng, Z. He, P. Ma, Z. Hou, K. Kim, J. Lu, K. Yang, G. Wang, X. Wang, Engineering neuroregenerative microenvironment via aligned hydrogel-assisted magnetic stimulation for complete spinal cord injury repair, *Engineered Regeneration* 5 (2) (2024) 139–152.
- [36] K. Yang, J. Yang, W. Man, Z. Meng, C.-Y. Yang, Z. Cao, J. Liu, K. Kim, Y. Liu, S. Yang, N-cadherin-functionalized nanofiber hydrogel facilitates spinal cord injury repair by building a favorable niche for neural stem cells, *Advanced Fiber Materials* 5 (4) (2023) 1349–1366.
- [37] Y. Cao, B. Chen, Q. Liu, Y. Mao, Y. He, X. Liu, X. Zhao, Y. Chen, X. Li, Y. Li, L. Liu, C. Guo, S. Liu, F. Tan, H. Lu, J. Liu, C. Chen, Dissolvable microneedle-based wound dressing transdermally and continuously delivers anti-inflammatory and pro-angiogenic exosomes for diabetic wound treatment, *Bioact. Mater.* 42 (2024) 32–51.
- [38] W. Man, S. Yang, Z. Cao, J. Lu, X. Kong, X. Sun, L. Zhao, Y. Guo, S. Yao, G. Wang, X. Wang, A multi-modal delivery strategy for spinal cord regeneration using a composite hydrogel presenting biophysical and biochemical cues synergistically, *Biomaterials* 276 (2021) 120971.
- [39] W. Man, S. Yang, Z. Cao, J. Lu, X. Kong, X. Sun, L. Zhao, Y. Guo, S. Yao, G. Wang, A multi-modal delivery strategy for spinal cord regeneration using a composite hydrogel presenting biophysical and biochemical cues synergistically, *Biomaterials* 276 (2021) 120971.

- [40] S. Yao, X. Liu, S. Yu, X. Wang, S. Zhang, Q. Wu, X. Sun, H. Mao, Co-effects of matrix low elasticity and aligned topography on stem cell neurogenic differentiation and rapid neurite outgrowth, *Nanoscale* 8 (19) (2016) 10252–10265.
- [41] S. Yang, J. Zhu, C. Lu, Y. Chai, Z. Cao, J. Lu, Z. Zhang, H. Zhao, Y.Y. Huang, S. Yao, X. Kong, P. Zhang, X. Wang, Aligned fibrin/functionalized self-assembling peptide interpenetrating nanofiber hydrogel presenting multi-cues promotes peripheral nerve functional recovery, *Bioact. Mater.* 8 (2022) 529–544.
- [42] K. Nagase, H. Wakayama, J. Matsuda, N. Kojima, H. Kanazawa, Thermoresponsive mixed polymer brush to effectively control the adhesion and separation of stem cells by altering temperature, *Materials Today Bio* 20 (2023) 100627.
- [43] P. Ma, C.-Y. Yang, C. Li, P. Hu, F. Yang, J. Lu, Y.-Y. Huang, H. Wu, Q. Wu, Y. Pan, Blow-spun Si3N4-incorporated nanofibrous dressing with antibacterial, anti-inflammatory, and angiogenic activities for chronic wound treatment, *Advanced Fiber Materials* 6 (2) (2024) 543–560.
- [44] O. Chaudhuri, J. Cooper-White, P.A. Janmey, D.J. Mooney, V.B. Shenoy, Effects of extracellular matrix viscoelasticity on cellular behaviour, *Nature* 584 (7822) (2020) 535–546.
- [45] A. Saraswathibhatla, D. Indana, O. Chaudhuri, Cell–extracellular matrix mechanotransduction in 3D, *Nat. Rev. Mol. Cell Biol.* 24 (7) (2023) 495–516.
- [46] U. Blache, E.M. Ford, B. Ha, L. Rijns, O. Chaudhuri, P.Y.W. Dankers, A.M. Kloxin, J. G. Snedeker, E. Gentleman, Engineered hydrogels for mechanobiology, *Nature Reviews Methods Primers* 2 (1) (2022) 98.
- [47] Y. Li, Z. Xiao, Y. Zhou, S. Zheng, Y. An, W. Huang, H. He, Y. Yang, S. Li, Y. Chen, J. Xiao, J. Wu, Controlling the multiscale network structure of fibers to stimulate wound matrix rebuilding by fibroblast differentiation, *ACS Appl. Mater. Interfaces* 11 (31) (2019) 28377–28386.
- [48] K. Holmes, O.L. Roberts, A.M. Thomas, M.J. Cross, Vascular endothelial growth factor receptor-2: structure, function, intracellular signalling and therapeutic inhibition, *Cell. Signal.* 19 (10) (2007) 2003–2012.
- [49] Y. Ge, Q. Wang, Y. Yao, Q. Xin, J. Sun, W. Chen, Y. Lin, X. Cai, Framework nucleic acids-based VEGF signaling activating system for angiogenesis: a dual stimulation strategy, *Adv. Sci.* 11 (21) (2024) 2308701.
- [50] Y. Zou, W. Chen, J. Chen, Z. You, Vascular endothelial growth factor receptor 1 facilitates the effect of macrophages on human umbilical vein endothelial cells migration by regulating the M1 polarization, *J. Biomed. Nanotechnol.* 18 (12) (2022) 2839–2845.
- [51] Y. Huang, K. Ye, A. He, S. Wan, M. Wu, D. Hu, K. Xu, P. Wei, J. Yin, Dual-layer conduit containing VEGF-A–Transfected Schwann cells promotes peripheral nerve regeneration via angiogenesis, *Acta Biomater.* 180 (2024) 323–336.
- [52] J. Hwang, K.L. Kiick, M.O. Sullivan, VEGF-encoding, gene-activated collagen-based matrices promote blood vessel formation and improved wound repair, *ACS Appl. Mater. Interfaces* 15 (13) (2023) 16434–16447.
- [53] F. Huang, X. Lu, Y. Yang, Y. Yang, Y. Li, L. Kuai, B. Li, H. Dong, J. Shi, Microenvironment-based diabetic foot ulcer nanomedicine, *Adv. Sci.* 10 (2) (2023) 2203308.
- [54] D. Ribatti, B. Nico, E. Crivellato, Morphological and molecular aspects of physiological vascular morphogenesis, *Angiogenesis* 12 (2009) 101–111.
- [55] I. Appelmann, R. Liersch, T. Kessler, R.M. Mesters, W.E. Berdel, Angiogenesis inhibition in cancer therapy: platelet-derived growth factor (PDGF) and vascular endothelial growth factor (VEGF) and their receptors: biological functions and role in malignancy, *Angiogenesis Inhibition* (2010) 51–81.
- [56] N. Tran, T. Garcia, M. Aniq, S. Ali, A. Ally, S.M. Nauli, Endothelial nitric oxide synthase (eNOS) and the cardiovascular system: in physiology and in disease states, *American journal of biomedical science & research* 15 (2) (2022) 1523.
- [57] E.L. Mills, B. Kelly, A. Logan, A.S. Costa, M. Varma, C.E. Bryant, P. Tourlomousis, J. H.M. Däbritz, E. Gottlieb, I. Latorre, Succinate dehydrogenase supports metabolic repurposing of mitochondria to drive inflammatory macrophages, *Cell* 167 (2) (2016) 457–470.
- [58] S.A. Eming, T.A. Wynn, P. Martin, Inflammation and metabolism in tissue repair and regeneration, *Science* 356 (6342) (2017) 1026–1030.
- [59] Y. Xu, Q. Saïding, X. Zhou, J. Wang, W. Cui, X. Chen, Electrospun fiber-based immune engineering in regenerative medicine, *Smart Medicine* 3 (1) (2024) e20230034.
- [60] M. Kharaziha, A. Baidya, N. Annabi, Rational design of immunomodulatory hydrogels for chronic wound healing, *Adv. Mater.* 33 (39) (2021) 2100176.
- [61] X. Dong, S. Liu, Y. Yang, S. Gao, W. Li, J. Cao, Y. Wan, Z. Huang, G. Fan, Q. Chen, H. Wang, M. Zhu, D. Kong, Aligned microfiber-induced macrophage polarization to guide schwann-cell-enabled peripheral nerve regeneration, *Biomaterials* 272 (2021) 120767.
- [62] T.A. Wynn, A. Chawla, J.W. Pollard, Macrophage biology in development, homeostasis and disease, *Nature* 496 (7446) (2013) 445–455.
- [63] X. Dong, S. Liu, Y. Yang, S. Gao, W. Li, J. Cao, Y. Wan, Z. Huang, G. Fan, Q. Chen, Aligned microfiber-induced macrophage polarization to guide schwann-cell-enabled peripheral nerve regeneration, *Biomaterials* 272 (2021) 120767.
- [64] F.Y. McWhorter, T. Wang, P. Nguyen, T. Chung, W.F. Liu, Modulation of macrophage phenotype by cell shape, *Proc. Natl. Acad. Sci. USA* 110 (43) (2013) 17253–17258.
- [65] J. Van Snick, Interleukin-6: an overview, *Annu. Rev. Immunol.* 8 (1) (1990) 253–278.
- [66] R. Sabat, G. Grütz, K. Warszawska, S. Kirsch, E. Witte, K. Wolk, J. Geginat, Biology of interleukin-10, *Cytokine Growth Factor Rev.* 21 (5) (2010) 331–344.
- [67] V. Parfejevs, J. Debbache, O. Shakhova, S.M. Schaefer, M. Glausch, M. Wegner, U. Suter, U. Riektina, S. Werner, L. Sommer, Injury-activated glial cells promote wound healing of the adult skin in mice, *Nat. Commun.* 9 (1) (2018) 236.
- [68] S. Zhou, L. Wan, X. Liu, D. Hu, F. Lu, X. Chen, F. Liang, Diminished schwann cell repair responses play a role in delayed diabetes-associated wound healing, *Front. Physiol.* 13 (2022) 2701.
- [69] E. Zakin, R. Abrams, D.M. Simpson, Diabetic neuropathy, *Semin. Neurol.* 39 (5) (2019) 560–569.
- [70] Y. Wu, L. Wang, B. Guo, Y. Shao, P.X. Ma, Electroactive biodegradable polyurethane significantly enhanced schwann cells myelin gene expression and neurotrophin secretion for peripheral nerve tissue engineering, *Biomaterials* 87 (2016) 18–31.
- [71] Y. Gu, Y. Ji, Y. Zhao, Y. Liu, F. Ding, X. Gu, Y. Yang, The influence of substrate stiffness on the behavior and functions of schwann cells in culture, *Biomaterials* 33 (28) (2012) 6672–6681.
- [72] Y.H. Kim, Y.H. Kim, Y.K. Shin, Y.R. Jo, D.K. Park, M.Y. Song, B.A. Yoon, S.H. Nam, J.H. Kim, B.O. Choi, p75 and neural cell adhesion molecule 1 can identify pathologic schwann cells in peripheral neuropathies, *Annals of Clinical and Translational Neurology* 6 (7) (2019) 1292–1301.
- [73] S. Yang, C. Wang, J. Zhu, C. Lu, H. Li, F. Chen, J. Lu, Z. Zhang, X. Yan, H. Zhao, Self-assembling peptide hydrogels functionalized with LN-and BDNF-mimicking epitopes synergistically enhance peripheral nerve regeneration, *Theranostics* 10 (18) (2020) 8227.
- [74] Y. Xiong, Z. Lin, P. Bu, T. Yu, Y. Endo, W. Zhou, Y. Sun, F. Cao, G. Dai, Y. Hu, L. Lu, L. Chen, P. Cheng, K. Zha, M.-A. Shahbazi, Q. Feng, B. Mi, G. Liu, A whole-course-repair system based on neurogenesis-angiogenesis crosstalk and macrophage reprogramming promotes diabetic wound healing, *Adv. Mater.* 35 (19) (2023) 2212300.
- [75] G. Bussone, Subjectivity in primary headaches: insight the causes, *Neurol. Sci.* 38 (Suppl 1) (2017) 1–2.
- [76] H.E. desJardins-Park, D.S. Foster, M.T. Longaker, Fibroblasts and wound healing: an update, *Regen. Med.* 13 (5) (2018) 491–495.
- [77] H.E. Talbott, S. Mascharak, M. Griffin, D.C. Wan, M.T. Longaker, Wound healing, fibroblast heterogeneity, and fibrosis, *Cell Stem Cell* 29 (8) (2022) 1161–1180.
- [78] A. Jurisic, P.J. Sung, M. Wappett, J. Daubriac, I.T. Lobb, W.W. Kung, N. Crawford, N. Page, E. Cassidy, S. Feutren-Burton, J.S.S. Rountree, M.D. Helm, C.R. O’Dowd, R.D. Kennedy, G. Gavory, A.N. Cranston, D.B. Longley, X. Jacq, T. Harrison, USP7 inhibitors suppress tumour neoangiogenesis and promote synergy with immune checkpoint inhibitors by downregulating fibroblast VEGF, *Clin. Transl. Med.* 14 (4) (2024) e1648.
- [79] L. Benington, G. Rajan, C. Locher, L.Y. Lim, Fibroblast growth factor 2-A review of stabilisation approaches for clinical applications, *Pharmaceutics* 12 (6) (2020).
- [80] H. Kuivaniemi, G. Tromp, Type III collagen (COL3A1): gene and protein structure, tissue distribution, and associated diseases, *Gene* 707 (2019) 151–171.
- [81] M.V. Plikus, X. Wang, S. Sinha, E. Forte, S.M. Thompson, E.L. Herzog, R.R. Driskell, N. Rosenthal, J. Biernaskie, V. Horsley, Fibroblasts: origins, definitions, and functions in health and disease, *Cell* 184 (15) (2021) 3852–3872.
- [82] Y. Li, Z. Xiao, Y. Zhou, S. Zheng, Y. An, W. Huang, H. He, Y. Yang, S. Li, Y. Chen, J. Xiao, J. Wu, Controlling the multiscale network structure of fibers to stimulate wound matrix rebuilding by fibroblast differentiation, *ACS Appl. Mater. Interfaces* 11 (31) (2019) 28377–28386.
- [83] K. Francis, B.O. Palsson, Effective intercellular communication distances are determined by the relative time constants for cyto/chemokine secretion and diffusion, *Proc. Natl. Acad. Sci. USA* 94 (23) (1997) 12258–12262.
- [84] N. Mandakhbayar, Y. Ji, A. El-Fiqi, K.D. Patel, D.S. Yoon, K. Dashnyam, O. Bayaraa, G. Jin, K. Tsogtbaatar, T.-H. Kim, Double hits with bioactive nanozyme based on cobalt-doped nanoglass for acute and diabetic wound therapies through anti-inflammatory and pro-angiogenic functions, *Bioact. Mater.* 31 (2024) 298–311.
- [85] S.P. Cartland, M.S. Patil, E. Kelland, N. Le, L. Boccanfuso, C.P. Stanley, P. M. Cholan, M.I. Dona, R. Patrick, J. McGrath, The generation of stable microvessels in ischemia is mediated by endothelial cell derived TRAIL, *Sci. Adv.* 10 (40) (2024) eadn8760.
- [86] J. Lan, R. Zeng, Z. Li, X. Yang, L. Liu, L. Chen, L. Sun, Y. Shen, T. Zhang, Y. Ding, Biomimetic nanomodulators with synergism of photothermal therapy and vessel normalization for boosting potent anticancer immunity, *Adv. Mater.* (2024) 2408511.
- [87] N. Liu, S. Zhu, Y. Deng, M. Xie, M. Zhao, T. Sun, C. Yu, Y. Zhong, R. Guo, K. Cheng, Construction of multifunctional hydrogel with metal-polyphenol capsules for infected full-thickness skin wound healing, *Bioact. Mater.* 24 (2023) 69–80.
- [88] P. Betancur, M. Bronner-Fraser, T. Sauka-Spengler, Genomic code for Sox10 activation reveals a key regulatory enhancer for cranial neural crest, *Proc. Natl. Acad. Sci. USA* 107 (8) (2010) 3570–3575.
- [89] Y. Chai, H. Zhao, S. Yang, X. Gao, Z. Cao, J. Lu, Q. Sun, W. Liu, Z. Zhang, J. Yang, Structural alignment guides oriented migration and differentiation of endogenous neural stem cells for neurogenesis in brain injury treatment, *Biomaterials* 280 (2022) 121310.